

Numerical Calculations of the B_{1g} Raman Spectrum of the Two-Dimensional Heisenberg Model

Anders W. Sandvik

Department of Physics, University of Illinois at Urbana-Champaign, 1110 West Green Street, Urbana, Illinois 61801

Sylvain Capponi and Didier Poilblanc

Laboratoire de Physique Quantique and Unité Mixte de Recherche CNRS 5626, Université Paul Sabatier, 31062 Toulouse, France

Elbio Dagotto

National High Magnetic Field Laboratory, Florida State University, 1800 E. Paul Dirac Dr., Tallahassee, Florida 32306
(March 24, 2022)

The B_{1g} Raman spectrum of the two-dimensional $S = 1/2$ Heisenberg model is discussed within Loudon-Fleury theory at both zero and finite temperature. The exact $T = 0$ spectrum for lattices with up to 6×6 sites is computed using Lanczös exact diagonalization. A quantum Monte Carlo (QMC) method is used to calculate the corresponding imaginary-time correlation function and its first two derivatives for lattices with up to 16×16 spins. The imaginary-time data is continued to real frequency using the maximum-entropy method, as well as a fit based on spinwave theory. The numerical results are compared with spinwave calculations for finite lattices. There is a surprisingly large change in the exact spectrum going from 4×4 to 6×6 sites. In the former case there is a single dominant two-magnon peak at $\omega/J \approx 3.0$, whereas in the latter case there are two approximately equal-sized peaks at $\omega/J \approx 2.7$ and 3.9 . This is in good qualitative agreement with the spinwave calculations including two-magnon processes on the same lattices. The spinwave results for larger lattices show how additional peaks emerge with increasing lattice size, and eventually develop into the well known two-magnon profile peaked at $\omega/J \approx 3.2$ and with weight extending up to $\omega/J \approx 4.6$. Both the Lanczös and the QMC results indicate that the actual two-magnon profile is broader than the narrow peak obtained in spinwave theory, but the positions of the maxima agree to within a few percent. The higher-order contributions present in the numerical results are merged with the two-magnon profile and extend up to frequencies $\omega/J \approx 7$. The first three frequency cumulants of the spectrum are in excellent agreement with results previously obtained from a series expansion around the Ising limit. Typical experimental B_{1g} spectra for La_2CuO_4 are only slightly broader than what we obtain here. The exchange constant extracted from the peak position is $J \approx 1400\text{K}$, in good agreement with values obtained from neutron scattering and NMR experiments. We discuss the implications of our present results for more sophisticated theories of Raman scattering suggested recently.

PACS numbers: 75.40.Gb, 75.40.Mg, 75.10.Jm, 75.50.Ee

I. INTRODUCTION

The magnetic properties of the parent compounds of the high- T_c cuprate superconductors can be well accounted for by weakly coupled two-dimensional (2D) Heisenberg antiferromagnets.¹ Neglecting the weak inter-layer coupling, the model is defined by the Hamiltonian

$$\hat{H} = J \sum_{\langle i,j \rangle} \mathbf{S}_i \cdot \mathbf{S}_j, \quad (J > 0), \quad (1)$$

where \mathbf{S}_i is a spin-1/2 operator at site i on a square lattice and $\langle i,j \rangle$ denotes a pair of nearest-neighbor sites. The most well studied among the antiferromagnetic layered cuprates is La_2CuO_4 ,^{2,3,4,5,6} with a Néel ordering temperature $T_N \approx 300\text{K}$. For $T > T_N$, the temperature dependence of the spin correlation length, measured using neutron scattering,² is in good agreement with that

of a single-layer Heisenberg model with $J \approx 1500\text{K}$.^{7,8} The spinwave spectrum of the Heisenberg model is well reproduced over the entire Brillouin zone.^{3,9} The NMR relaxation rates $1/T_1$ and $1/T_{2G}$, which probe the low-frequency spin dynamics, also show remarkable agreement between experiment^{5,6} and theory.^{7,10,11,12}

In contrast to these success stories, the experimental Raman spectrum^{13,14,15} shows significant deviations from calculations for the 2D Heisenberg model.^{16,17,18,19} Within this description of the CuO_2 layers, the standard theory of Raman scattering is based on the Loudon-Fleury (LF) coupling²⁰ between the light and the spin system. The coupling is obtained in second order perturbation theory with virtual states containing one doubly occupied site, and is given by^{20,21}

$$\hat{H}_{LF} = \sum_{\langle i,j \rangle} (\mathbf{E}_{\text{in}} \cdot \sigma_{ij})(\mathbf{E}_{\text{out}} \cdot \sigma_{ij}) \mathbf{S}_i \cdot \mathbf{S}_j. \quad (2)$$

Here \mathbf{E}_{in} and \mathbf{E}_{out} are the polarization vectors of the incoming and scattered light and σ_{ij} is the unit vector connecting sites i and j . In terms of the eigenstates $\{|n\rangle\}$ of the Heisenberg model, the frequency dependence of the scattering intensity at inverse temperature β is given by Fermi's Golden Rule:

$$I(\omega) = \frac{1}{Z} \sum_m e^{-\beta E_m} \times \sum_n |\langle n | \hat{H}_{LF} | m \rangle|^2 \delta(\omega - [E_n - E_m]). \quad (3)$$

Most theoretical work has focused on the scattering in the B_{1g} symmetry channel. This corresponds to \mathbf{E}_{in} along a diagonal of the square lattice, and \mathbf{E}_{out} perpendicular to \mathbf{E}_{in} . The B_{1g} coupling can thus be written as

$$\hat{H}_{LF} = \sum_{\langle i,j \rangle_x} \mathbf{S}_i \cdot \mathbf{S}_j - \sum_{\langle i,j \rangle_y} \mathbf{S}_i \cdot \mathbf{S}_j, \quad (4)$$

where $\langle i,j \rangle_x$ and $\langle i,j \rangle_y$ denote links in the x and y directions, respectively.

For La_2CuO_4 , the B_{1g} spectrum has a broad asymmetric peak at $\omega \approx 3J$ with a tail extending to $\omega \approx 7 - 8J$.¹³ In some cases there is a shoulder-like structure at $\omega \approx 4J$. Within spinwave theory the B_{1g} scattering is dominated by two-magnon excitations. The two-magnon profile is peaked around $\omega \approx 3J$ in good agreement with the experiments.^{16,17,18,19} However, the large width of the experimental spectrum has not been reproduced within spinwave theory. The first three frequency cumulants of the spectrum have also been calculated using a series expansion around the Ising limit,²² and are in reasonable agreement with the experimental values. The moments obtained in spinwave theory to order $1/S$ (two magnon excitations only) are in poor agreement with the series results which in principle include multi-magnon contributions to all orders. Unfortunately, the full frequency dependence is not accessible with the series expansion method. Exact diagonalization has been used to compute the exact LF Raman profile for small lattices.¹⁹ For the 4×4 system there is a single dominant two-magnon peak at $\omega/J = 2.98$. Weight present at $\omega \approx 5J$ has been attributed to four-magnon processes, but its relative strength is much smaller than the weight found experimentally in this frequency region. The tail at higher frequencies is absent. Despite this, the first three frequency cumulants are in approximate agreement with both experiments and the series expansion results.

Canali and Girvin¹⁷ carried out a spin-wave expansion including also four-magnon excitations (which enter in order S^{-2}). The narrow width of the two-magnon peak was found to be stable with respect to inclusion of the higher-order processes. The relative contribution from four-magnon states in this calculation is less than 3%. The high energy of the four-magnon weight nevertheless leads to first and second cumulants that are much closer to those obtained in the series expansion and exact diagonalization studies. The spinwave result for the third

cumulant is, however, significantly larger than the series expansion value. It was argued that this is due to interactions between four magnons that were neglected in the $1/S^2$ calculation, and that the relative four-magnon contribution must be $\approx 10\%$ in order to reproduce the first three moments.¹⁷ The conclusion that there is less high-energy weight than in typical experimental spectra then still remains. However, the apparent inability of a very sophisticated spinwave calculation to fully capture the four-magnon processes raises some concerns about this approach for calculating the actual line shape. Furthermore, Chubukov and Frenkel have recently questioned the stage at which the spin S was set to $1/2$ in the previous spinwave calculations. They kept S large and carried out an expansion of the profile around its peak position before expanding in $1/S$ and evaluating the result at $S = 1/2$. The two-magnon profile obtained this way has a width almost three times larger than the “standard” one, and the second frequency cumulant is therefore in better agreement with the series result. However, the agreement with the first cumulant is actually worse, due to the significantly larger low-frequency weight. Hence, this result also has to be viewed with some caution.

Experimentally, significant scattering is also observed in the A_{1g} channel.¹³ With the standard LF coupling inelastic scattering in this symmetry is not possible for the Heisenberg model with only nearest-neighbor interactions, since the x and y terms in Eq. (4) are added in this case and \hat{H}_{LF} then commutes with the Hamiltonian. Adding a next-nearest-neighbor term to the LF coupling leads to A_{1g} scattering, but has no effect in the B_{1g} channel.²² Based on the frequency moments obtained in the series expansion, this was argued to be a mechanism that could explain both the B_{1g} and A_{1g} spectra. However, the narrow B_{1g} line-shape obtained in other calculations remains an unresolved issue for this scenario. Including a next-nearest-neighbor term $\sim J_2$ in the Hamiltonian would also lead to A_{1g} scattering, and probably a broadened B_{1g} spectrum. The relatively large A_{1g} intensity seen experimentally would then likely require a larger J_2 than allowed by other experiments, but detailed calculations have not been carried out within this model. Other interactions, such as the so called four-spin cyclical exchange,^{18,23} have also been suggested to account for the differences between theory and experiment. Analytical calculations as detailed as those for the standard LF theory (only nearest-neighbor interactions in both the Hamiltonian and the Raman operator) have also not yet been carried out within these theories.

It is clear that LF theory is not sufficient to capture all aspects of Raman scattering in layered cuprates. For example, resonant scattering (occurring when the frequency of the incoming light is comparable to the charge-transfer gap) can of course not occur within the Heisenberg model.²⁴ However, focusing on nonresonant B_{1g} scattering, it is not yet clear what the actual line shape is within LF theory. As discussed above, the two key

questions of the width of the dominant two-magnon profile and the relative weight of the higher-order contributions above the two-magnon cut-off remain incompletely answered within spinwave theory. The exact diagonalization studies carried out so far are limited to lattices too small for reliable quantitative extrapolation to the thermodynamic limit. There is hence a definite need for accurate non-perturbative numerical calculations for larger lattices. Conclusive results would provide a more solid basis for estimating effects not included in the LF-Heisenberg model. It should also be noted that LF theory is the standard framework in which Raman scattering has been interpreted also in several other low-dimensional antiferromagnetic $S = 1/2$ systems.^{25,26} A satisfactory resolution of the 2D Heisenberg case would therefore be of more general interest as well. Finally, knowing the exact B_{1g} Raman spectrum should help to shed light on the applicability of spinwave theory for calculations of dynamic processes involving excitations of more than one magnon.

Here we report new exact diagonalization results for systems with up to 6×6 spins, which is the largest currently accessible with this method. We also obtain approximate spectra for up to 16×16 spins by Maximum-Entropy (Max-Ent) analytic continuation of quantum Monte Carlo (QMC) data. Using the stochastic series expansion QMC technique^{27,28,29} we have calculated the imaginary-time LF correlation function and its first two derivatives at temperatures low enough to give ground state results. The derivatives are used as supplementary information in the analytic continuation. We also consider a more phenomenological approach of fitting the two-magnon profile obtained within spinwave theory to the imaginary-time data, adding a Gaussian at higher frequency to model the higher-order contributions. In order to study the effects of temperature, we apply the QMC + Max-Ent methods also at non-zero temperatures.

We find that the B_{1g} Raman spectrum of the 6×6 lattice has two dominant peaks at $\omega/J \approx 2.7$ and 3.9 , in sharp contrast to the single dominant peak at $\omega/J = 2.98$ previously found for the 4×4 lattice. These results are qualitatively reproduced within spin wave theory including only two-magnon excitations and magnon-magnon interactions (treated within an RPA scheme). Spinwave results resembling the infinite-size two-magnon profile are seen only for much larger lattices. Using the QMC data, the first three frequency cumulants in the thermodynamic limit can be reliably estimated. They are in excellent agreement with the previous series expansion results.²² Both the Lanczös and the QMC results indicate that the dominant peak at $\omega \approx 3.3J$ is slightly broader than the standard two-magnon profile, but not as broad as the one recently obtained by Chubukov and Frenkel.²⁴ We find no evidence for a gap between the two-magnon profile and the higher-order contributions. They appear to be completely merged together and extend up to $\omega \approx 7J$.

Finite-temperature results for $T/J \lesssim 0.25$ are very

similar to the ground state results. For higher temperatures there is a significant growth of the low-frequency spectral weight, as also found in a previous exact diagonalization study of a 4×4 lattice.³⁰ We find that the temperature at which this effect becomes significant decreases with increasing system size, due to the large finite-size gaps present in the smaller systems.

Over-all, our results are in closer agreement with experiments than previous exact diagonalization and spin-wave calculations, but we conclude that the Heisenberg-LF spectrum is nevertheless not quite as broad as typical experimental spectra. We argue that our results give more credibility to proposed broadening mechanisms involving phonons.^{14,31,32,33,34}

The rest of the paper is organized as follows. In Sec. II we review various spinwave calculations of the B_{1g} Raman profile. We also present results for small lattices, which are compared with exact diagonalization spectra in Sec. III. Our $T = 0$ results from QMC simulation and numerical analytic continuation are discussed in Sec. IV. Effects of finite temperature are considered in Sec. V. In Sec. VI we summarize and discuss our results and implications for mechanisms proposed to lead to a broadening of the B_{1g} profile. In an Appendix we present some technical details of the QMC calculation of the imaginary-time correlation function and its derivatives.

II. SPINWAVE THEORY

The Raman spectrum can be easily computed in the spinwave approximation. Various improvements of the linear spinwave calculation can be also applied to the Raman scattering amplitude. For example, the residual interactions between spin waves, which play a crucial role in the Raman excited states, can be included at the RPA level. Here we discuss linear spin wave theory and the effect of magnon-magnon interactions on the B_{1g} spectrum. The primary purpose of the calculations discussed here is to qualitatively understand the effects of finite size, which will be important for interpreting the numerical results presented in the following sections. More sophisticated spinwave calculations including the quantum fluctuations of the ground state, as well as final states with four magnons, have been carried out before, as discussed in the Introduction. Here we note some problems with the analytical calculations of the Raman profile which motivate our renewed efforts to obtain accurate non-perturbative numerical results.

In the antiferromagnetic ground state we are considering, a bosonic representation of the spin operators can be introduced on each sublattice by using the usual Dyson-Maleev transformation^{35,36}. On sublattice A , the transformation reads

$$S_i^z = S - a_i^\dagger a_i \quad (5a)$$

$$S_i^+ = \sqrt{2S} \left(1 - \frac{a_i^\dagger a_i}{2S} \right) a_i \quad (5b)$$

$$S_i^- = \sqrt{2S}a_i^\dagger, \quad (5c)$$

where a_i^\dagger creates a boson, i.e., a spin-1 magnon, at site i . Similarly, on sublattice B ,

$$S_j^z = -S + b_j^\dagger b_j \quad (6a)$$

$$S_j^+ = \sqrt{2S}b_j^\dagger \left(1 - \frac{b_j^\dagger b_j}{2S}\right) \quad (6b)$$

$$S_j^- = \sqrt{2S}b_j. \quad (6c)$$

As usual, as long as small fluctuations around the Néel ordered phase are considered, one keeps only quadratic terms in the Hamiltonian (which are the dominant terms in a $1/S$ expansion). Therefore, in this approximation, the Hamiltonian can be diagonalized by a Bogoliubov transformation in terms of spinwave excitations (or magnons);

$$\alpha_{\mathbf{k}} = u_{\mathbf{k}}a_{\mathbf{k}} + v_{\mathbf{k}}b_{\mathbf{k}}^\dagger \quad (7a)$$

$$\beta_{\mathbf{k}} = u_{\mathbf{k}}b_{\mathbf{k}} + v_{\mathbf{k}}a_{\mathbf{k}}^\dagger, \quad (7b)$$

where the coefficients (> 0) are given by,

$$u_{\mathbf{k}}^2 = \frac{1}{2} \left(\frac{1}{\sqrt{1-\gamma_{\mathbf{k}}^2}} + 1 \right) \quad (7c)$$

$$v_{\mathbf{k}}^2 = \frac{1}{2} \left(\frac{1}{\sqrt{1-\gamma_{\mathbf{k}}^2}} - 1 \right). \quad (7d)$$

We have defined $\gamma_{\mathbf{k}} = \sum_{\delta} e^{i\mathbf{k}\cdot\delta}/Z$ as a sum over the Z nearest neighbours of the site at the origin. In our case (square lattice), $\gamma_{\mathbf{k}} = (\cos k_x + \cos k_y)/2$. The resulting well known linear spinwave Hamiltonian reads,

$$H_{SW} = E_0 + \sum_{\mathbf{k}} \omega_{\mathbf{k}} (\alpha_{\mathbf{k}}^\dagger \alpha_{\mathbf{k}} + \beta_{\mathbf{k}}^\dagger \beta_{\mathbf{k}}), \quad (8)$$

with the dispersion relation $\omega_{\mathbf{k}} = JSZ\sqrt{1-\gamma_{\mathbf{k}}^2}$. Due to the decomposition into two sublattices, the reciprocal space is reduced to the magnetic brillouin zone (MBZ).

The LF operator can be easily expressed as a quadratic form in terms of the spin wave operators. At zero temperature the ground state contains no bosons if magnon-magnon interactions are neglected so that, in a first approximation, one only keeps constant terms or terms involving the creation of magnons, giving

$$H_{LF} = -\alpha N S^2 \mathbf{E}_{\text{out}} \cdot \mathbf{E}_{\text{in}} \quad (9)$$

$$+ 2\alpha S \sum_{\mathbf{k}} \left(E_{\text{out}}^x E_{\text{in}}^x [\cos k_x (u_{\mathbf{k}}^2 + v_{\mathbf{k}}^2) - 2u_{\mathbf{k}} v_{\mathbf{k}}] \right) \quad (10)$$

$$+ E_{\text{out}}^y E_{\text{in}}^y [\cos k_y (u_{\mathbf{k}}^2 + v_{\mathbf{k}}^2) - 2u_{\mathbf{k}} v_{\mathbf{k}}] \alpha_{\mathbf{k}}^\dagger \beta_{\mathbf{k}}^\dagger. \quad (11)$$

In the B_{1g} geometry, the matrix element is thus

$$\langle f | H_R | i \rangle = \frac{\cos k_x - \cos k_y}{\sqrt{1-\gamma_{\mathbf{k}}^2}}. \quad (12)$$

The Raman intensity obtained from Fermi's Golden Rule, Eq. (3), is then

$$I(\omega) \propto \sum_{\mathbf{k}} \frac{(\cos k_x - \cos k_y)^2}{1-\gamma_{\mathbf{k}}^2} \delta(\omega - 2\Omega_{\mathbf{k}}), \quad (13)$$

where $\Omega_{\mathbf{k}} = 4JS\sqrt{1-\gamma_{\mathbf{k}}^2}$ is the frequency of the magnon. This expression exhibits a divergence at $\omega = 8JS$ since the density of states diverges at the boundary of the MBZ.

It is well known that this result is strongly modified when one takes into account the magnon-magnon interactions in the final state.^{37,16,17,24} In order $1/S$, the Dyson-Maleev transformation generates in the Hamiltonian quartic terms in the bosons operators. One way of treating this interaction is to keep the term $\alpha_{\mathbf{k}}^\dagger \beta_{\mathbf{k}}^\dagger \beta_{-\mathbf{p}} \alpha_{\mathbf{p}}$ ^{16,17,24} which is responsible for multiple scattering of two magnons in the vacuum. This part gives the dominant contribution to the magnon-magnon scattering coming from the region near the MBZ boundary where the density of states diverges. Further simplification results from the vanishing of $\gamma_{\mathbf{k}}$ at the MBZ boundary so that it is reasonable to replace $\gamma_{\mathbf{k}}$ by zero for all \mathbf{k} . This leads to an effective interaction of the form,²⁴

$$H_{\text{int}} = -\frac{4J}{N} \sum_{\mathbf{k}} \sum_{\mathbf{p}} \gamma_{\mathbf{k}-\mathbf{p}} \alpha_{\mathbf{k}}^\dagger \beta_{\mathbf{k}}^\dagger \beta_{-\mathbf{p}} \alpha_{\mathbf{p}}. \quad (14)$$

Following Refs. 24, 17 and expressing $\gamma_{\mathbf{k}-\mathbf{p}}$ as a function of its symmetric terms $\gamma_{\mathbf{k}-\mathbf{p}} = \gamma_{\mathbf{k}}^{c+} \gamma_{\mathbf{p}}^{c+} + \gamma_{\mathbf{k}}^{c-} \gamma_{\mathbf{p}}^{c-} + \gamma_{\mathbf{k}}^{s+} \gamma_{\mathbf{p}}^{s+} + \gamma_{\mathbf{k}}^{s-} \gamma_{\mathbf{p}}^{s-}$

$$\gamma_{\mathbf{k}}^{c\pm} = (\cos k_x \pm \cos k_y)/2 \quad (15)$$

$$\gamma_{\mathbf{k}}^{s\pm} = (\sin k_x \pm \sin k_y)/2, \quad (16)$$

it can be shown that multiple diffusion RPA series only contains terms involving $\gamma_{\mathbf{p}}^{c-}$ factors. The final RPA expression for the Raman intensity is given by,²⁴

$$I(\omega) \propto \text{Im} \left\{ \frac{R(\omega)}{1 + R(\omega)/4S} \right\} \quad (17)$$

with

$$R(\omega) = \frac{8JS}{N} \sum_{\mathbf{k}} \frac{(\cos k_x - \cos k_y)^2}{\omega - 2\Omega_{\mathbf{k}} + i\varepsilon}. \quad (18)$$

In the thermodynamic limit, Eq. (18) for $S = 1/2$ leads to a narrow two-magnon peak around $\omega = 2.78J$ which extends up to $\omega/J = 4$. In order to be able to directly compare spinwave results with exact spectra obtained with the Lanczös diagonalization method and approximate results of QMC and Max-Ent analytic continuation (presented in the following two sections), we have also evaluated (17) for small lattices. Results for $L \times L$ clusters with $L = 4, 6, 8$ and 10 are shown in Fig. 1, along with the corresponding non-interacting form (13). It is

clear that the continuous absorption band for infinite size is obtained from the accumulation of a series of peaks for increasing cluster sizes. However, the number of peaks is still very small even for a lattice of 100 sites.

In the above calculation the magnon-magnon interactions have only been included in the final two-magnon state. The main effect of interactions in the ground state is to renormalize the spinwave velocity; $c \rightarrow Z_c c$, where to order $1/S$ the renormalization factor $Z_c = 1.158$ and arises solely from the normal ordering of the quartic magnon terms.³⁸ Hence, in a phenomenological way, the $1/S$ corrections can be taken into account by shifting the energy scale by a factor Z_c , leading to a B_{1g} profile peaked at $\omega/J = 3.22$. However, Canali and Girvin have shown that the renormalization in fact enters in a non-trivial way in the expression for the Raman profile, and hence there are other effects as well.¹⁷ Nevertheless, the end result for $S = 1/2$ does not differ much from Eq. (18) with $Z_c = 1.158$, as shown in Fig. 1.

Chubukov and Frenkel have recently raised questions about the stage at which one should set $S = 1/2$ in the spinwave calculation. They argued that one should first expand the large- S expression for the profile (17) around its peak position, and only after that set $S = 1/2$.²⁴ The position of the maximum then remains approximately the same, but the profile is considerably broader, as also shown in Fig. 2. The better agreement with the frequency moments calculated by Singh *et al.*²² was used as support in favor of the broader peak. However, it should be noted that the agreement with the first cumulant is actually significantly worse, due to the much slower decay of the weight on the low-frequency side of the peak. In fact, as seen in Fig. 2, the Chubukov-Frenkel profile extended towards lower frequencies in a way similar to the experimental spectrum, but the high-frequency tail is still of course missing. The high-frequency scattering was argued to be dominated by resonant scattering in typical experimental situations, and would hence not be explainable by LF theory.²⁴

To higher orders in $1/S$, states enter in which 4, 6, e.t.c., magnons are excited (the true ground state is a linear combination of states containing any even number of magnons, and the Raman operator can create or annihilate one or two pairs of magnons). Canali and Girvin included four-magnon excitations (order $1/S^2$) but neglected interactions involving more than two magnons.¹⁷ The two-magnon profile obtained this way is very similar to the Canali-Girvin $1/S$ result discussed above. The relative contribution from four-magnon processes is less than 3%, but is likely strongly affected by the neglected interactions.¹⁷ In fact, although the small four-magnon contribution is sufficient (because of its rather high energy) to change the first and second frequency cumulants to values in close agreement with the series expansion results, the third cumulant remains far off. It was argued that this inconsistency is due to the neglected interactions among four magnons (which may even lead to bound states), and that such interactions would bring

the four-magnon peak position down in frequency.¹⁷ The relative four-magnon weight would then have to increase to $\approx 10\%$ in order to satisfy the first three moments. In our opinion, this rough estimate indicates that the approximations made in the $1/S^2$ calculation may in fact be serious. In particular, it is not clear that the two-magnon and four-magnon contributions will be well separated from each other if the four-magnon weight moves down and increases by a factor of 3 or more. This, in turn, may lead to considerably stronger interference effects that may cause changes also to the upper edge of the two-magnon profile (which then no longer would arise from two-magnon excitations only).

There are hence two major concerns with the spinwave calculations that have to be addressed: 1) The stage at which S is set to $1/2$, leading to two very different two-magnon line shapes. 2) The contributions from processes including four or more magnons, which are very difficult to capture completely within spinwave theory. In this situation it is clearly useful to consider non-perturbative numerical methods. We discuss two complementary approaches in the next two sections.

III. EXACT DIAGONALIZATION

In this section, we compute the exact Raman spectrum on clusters with up to $N = 36$ sites by use of the Lancz s diagonalization algorithm. In this approach, the Raman spectrum is obtained from a continued fraction,

$$I(\omega) = -\frac{1}{\pi} \text{Im} \left\{ \langle 0 | \hat{H}_{LF}^\dagger \frac{1}{\omega + E_0 + i\varepsilon - \hat{H}} \hat{H}_{LF} | 0 \rangle \right\}, \quad (19)$$

where $|0\rangle$ is the ground state of energy E_0 which can be easily calculated with the Lancz s method, and ε is a small imaginary part added to give a finite damping of the δ -functions.

Results for several square and tilted lattices are shown in Fig. 3, along with the RPA spinwave results discussed in the previous section. We have shifted the spinwave results by the renormalization factor $Z_c = 1.18$ obtained using several different numerical methods^{39,29} (this value is also in close agreement with the $1/S^2$ spinwave value $Z_c = 1.177$ ¹⁷). Spin wave theory clearly correctly predicts the number of the dominant peaks, which hence can be characterized as two-magnon peaks. There are, however, some discrepancies in the peak positions and their relative weights. Most notably, for the largest lattice (6×6), the separation between the two peaks in the exact spectrum exceeds by a factor of more than 1.5 that of the spinwave result. This may well be an indication that the correct two-magnon profile is broader than the standard profile obtained with spinwave theory.^{16,17} Whether or not it is as broad as that obtained by Chubukov and Frenkel (see Fig. 2) cannot be determined from the results for these small lattices, however. We will return to this important issue in the next section.

It can be noted that for the 4×4 lattice there is a small peak at $\omega/J \approx 4.5$ both in the spinwave and the Lancz s results. This then suggests that it is a two-magnon peak, in contrast to previous claims that it arises from a four-magnon state.¹⁹ For the larger lattices there is visible weight extending up to $\omega/J \approx 7$, which is not present in the spinwave results and hence is due to processes involving more than two magnons. For the 6×6 lattice the relative weight of these contributions is about 10%.

It is difficult to scale the full shape of the spectrum to infinite system size. The first few frequency cumulants can be expected to converge rather quickly, however, and have also previously been calculated using a series expansion method as already discussed. The n th frequency *moment* is given by (at $T = 0$)

$$\rho_n = \int_0^\infty d\omega \omega^n I(\omega). \quad (20)$$

The first cumulant $M_1 = \rho_1$, and for $n > 1$,

$$(M_n)^n = \frac{1}{\rho_0} \int_0^\infty d\omega (\omega - \rho_1)^n I(\omega). \quad (21)$$

The results for 6×6 (4×4) are $M_1 = 3.524$ (3.244), $M_2 = 0.8686$ (0.797), and $M_3 = 0.9576$ (1.141). The previous series expansion results²² are $M_1 = 3.58 \pm 0.06$, $M_2 = 0.81 \pm 0.05$, and $M_3 = 1.00 \pm 0.14$. Hence, the 6×6 cumulants show an improved and good agreement with the series results. However, since there are significant differences between the 4×4 and the 6×6 lattices, the results may still change in the thermodynamic limit. Unfortunately, using also the results for $N = 26$ and 32 , the data do not fall on smooth curves (see Fig. 8 in the next Section), and it is not possible to extrapolate to the thermodynamic limit using only these Lancz s results. In the next Section we will calculate the cumulants for much larger systems using QMC data.

IV. QUANTUM MONTE CARLO AND MAXIMUM-ENTROPY ANALYTIC CONTINUATION

Real-frequency dynamic properties cannot be obtained directly using QMC methods. Instead, the corresponding imaginary-time dependent correlation function has to be calculated, and numerically continued to real frequency. For the Raman spectrum defined by Eq. (3), the imaginary-time function is given by

$$G(\tau) = \langle \hat{H}_{LF}(\tau) \hat{H}_{LF}(0) \rangle, \quad (22)$$

where $\hat{H}_{LF}(\tau) = e^{\tau \hat{H}} \hat{H}_{LF} e^{-\tau \hat{H}}$. The analytic continuation to real frequency amounts to inverting the integral relation

$$G(\tau) = \frac{1}{\pi} \int_{-\infty}^{\infty} d\omega I(\omega) e^{-\tau \omega}. \quad (23)$$

With $G(\tau)$ obtained only to within a statistical error from a QMC simulation, the spectrum $I(\omega)$ cannot be uniquely determined. In the Max-Ent approach to this difficult problem,^{40,41} a unique solution is defined as that minimizing

$$Q = \frac{1}{2} \chi^2 - \alpha S, \quad (24)$$

where S is the entropy of the spectrum,

$$S = - \int_{-\infty}^{\infty} d\omega I(\omega) \ln [I(\omega)/m(\omega)], \quad (25)$$

defined with respect to a “default” model m (both I and m are here assumed to be normalized to unity). $G(\tau)$ is calculated for a discrete set of times τ_i . A given $I(\omega)$ corresponds to unique values of $G(\tau_i)$ according to Eq. (23). The deviation from the actual calculated $G_{\text{QMC}}(\tau_i)$ is quantified by χ^2 . Since the statistical errors σ_i of $G_{\text{QMC}}(\tau_i)$ at different times are correlated (see Fig. 13 in Appendix A), χ^2 should be defined in terms of the inverse of the full covariance matrix C ,

$$\chi^2 = \sum_{i,j} [G(\tau_i) - G_{\text{QMC}}(\tau_i)] C_{ij}^{-1} [G(\tau_j) - G_{\text{QMC}}(\tau_j)]. \quad (26)$$

We here parametrize the spectrum in terms of $N_\omega \sim 200 - 400$ equally spaced delta-functions $\delta(\omega - \omega_i)$ for $\omega_i > 0$:

$$I(\omega) = \sum_{i=1}^{N_\omega} I_i \delta(\omega_i - \omega), \quad (27)$$

and a smooth continuous spectrum is then represented by the curve connecting the amplitudes I_i (or by giving the δ -functions a width of the order of the frequency spacing, which gives a very similar curve). The negative part of the bosonic spectrum is given by detailed balance: $I(-\omega) = e^{-\beta \omega} I(\omega)$. We use a flat default model for $\omega > 0$. The parameter α in Eq. (24) is determined iteratively so as to satisfy the “classic” Max-Ent criterion, resulting in (within the assumptions of the Max-Ent method) the spectrum with the highest probability given the QMC data.

For calculating $G(\tau_i)$ we use the stochastic series expansion QMC method,^{27,28} as discussed in Appendix A. With this method, derivatives of $G(\tau)$ can also be directly calculated. We here use the first two derivatives as supplementary information in the Max-Ent method. The n th derivative of $G(\tau)$ is related to $I(\omega)$ according to

$$G^{(n)}(\tau) = \frac{(-1)^n}{\pi} \int_{-\infty}^{\infty} d\omega \omega^n I(\omega) e^{-\tau \omega}. \quad (28)$$

It is a straight-forward matter to modify the Max-Ent procedures to include also the first few (in our case 2)

of these derivative relations in addition to the original analytic continuation equation (23). The use of derivatives was first suggested by Schüttler and Scalapino in their pioneering work on numerical analytic continuation based on χ^2 fitting to QMC data.⁴² To our knowledge, the Max-Ent method has not previously been used with derivative information. It should be noted that the n th frequency moment ρ_n is given by the $\tau = 0$ derivative:

$$\rho_n = (-1)^n \frac{G^{(n)}(\tau \rightarrow 0)}{G(\tau \rightarrow 0)}. \quad (29)$$

Enforcing known frequency moments has been previously used to improve the resolution of the Max-Ent method.⁴³ The derivative information goes beyond this by enforcing also the “moments” defined with $\tau > 0$ in Eq. (29). The derivatives can of course be expected to improve on the Max-Ent procedure only if they can be calculated accurately enough to contain information not already present in the calculated $G(\tau)$. Typically, the statistical errors increase with increasing derivative order n . In our case, the first two derivatives appear to be useful, although spectra obtained with only $G(\tau)$ are not dramatically different.

Next, we present results for systems of size $L \times L$, with $L = 4, 6, 8$, and 10 . Although considerably larger lattices can be studied with the QMC method, the physical information we are interested in here requires very accurate results for $G(\tau)$. It is therefore more appropriate to concentrate the computational resources on obtaining reliable results for moderate system sizes. Comparing results for $L = 4 - 10$ should also be sufficient for making statements about the thermodynamic limit. We also carried out some simulations for $L = 16$, but the statistical error are significantly larger in this case and the continuation to real frequency is therefore less reliable. In order to obtain ground state results, the simulations were carried out at inverse temperatures as high as $\beta = 8L$. Results obtained with $\beta = 4L$ are indistinguishable within statistical errors, indicating that contributions from excited states indeed are negligible at these low temperatures.

We begin by showing in Fig. 4 our results for the logarithm of the normalized imaginary-time correlator $g(\tau) = G(\tau)/G(0)$. In the same figure we also show the relative statistical error, $\sigma_{\text{rel}}(\tau)$, of $g(\tau)$. Since the results for all the system sizes have comparable errors, one can expect the Max-Ent continuation to real frequency to resolve structure on roughly the same scale. Already from this imaginary-time data it is clear that the real-frequency spectrum has dominant weight at $\omega \approx 3J$ for all system sizes, as $\ln[g(\tau)]$ decays approximately linearly with τ in a sizable regime, with slope ≈ -3 . For the larger systems a slight upward curvature can be noted, indicating that there is spectral weight also below $3J$.

We find that the shape of the Raman spectrum obtained with the Max-Ent method is very sensitive to the statistical fluctuations in the QMC data. Carrying out the Max-Ent procedures with different subsets of the

available imaginary-time data always gives a dominant peak close to $\omega/J = 3$, but the peak width and asymmetry show large variations. We therefore consider it appropriate to define the spectrum corresponding to the full set of imaginary time data as an average over suitably defined subsets. For this purpose we use the so called bootstrap method⁴⁴ in the following way.

With the simulation data for some quantity A divided into M “bin averages” A_i in the standard way, a bootstrap sample A_B is defined as

$$A_B = \frac{1}{M} \sum_{i=1}^M A_{R_i}, \quad (30)$$

where R_i is a randomly chosen bin (i.e., the number of bins chosen is the same as the total number of bins, allowing, of course, for multiple selections the bins). Since the Max-Ent procedure is highly non-linear, the average over a large number of separately Max-Ent continued bootstrap samples of imaginary-time correlation functions can be different from the continued full average. We argue that the bootstrap average is more meaningful since statistical fluctuations are averaged out considerably.

In Fig. 5 we show Max-Ent results for 10 bootstrap samples of 4×4 QMC data. All the spectra have a dominant peak very close to the correct position $\omega/J = 2.98$, as well as a structure at higher frequency. There are, however, very large variations in the peak width and in the position of the high-frequency weight. The average over 500 bootstrap samples is shown in Fig. 6. The exact Lanczös result with a damping $\epsilon/J = 0.1$ is quite well reproduced, except that the small peak at $\omega/J = 4.5$ is not present. It can be noted that the main peak of the average spectrum is narrower than most of the “typical” bootstrap samples (see Fig. 5), contrary to what might have been expected. This is clearly due to the fact that the position of the peak shows very small variations compared to the variations in the peak width and that for some bootstrap samples the peak is very sharp.

Results for the larger lattices are also shown in Fig. 6. In the 6×6 spectrum the two main peaks are clearly resolved. The weight present at higher frequency cannot be resolved as a separate structure, however, and instead causes the shift by $\approx 15\%$ of the second peak. As the system size grows, the number and density of peaks increase, and only a single structure can then be resolved. For the 8×8 lattice, the spinwave result shown in Fig. 1 has only one dominant peak. The Max-Ent result for this size is, however, very broad, indicating that the relative weight distribution among the peaks obtained in spinwave theory is not reliable (signs of this is seen also in the exact 6×6 spectrum in Fig. 3). In particular, the Max-Ent spectrum has much more low-frequency weight. This is the case also for the 10×10 lattice. The spectrum has a more pronounced peak than for 8×8 , indicating that the individual δ -functions begin to group into a profile peaked around $\omega/J \approx 3.5$. It should be noted that the procedures we are using can be expected to work better

for the larger systems, for which the distribution of δ -functions are better approximated by a single continuous structure.

In Fig. 7 we show the results for the short-time behavior of the ratio $G^{(n)}(\tau)/G(\tau)$, along with the corresponding curves obtained from the Max-Ent results. According to Eq. (29), the first two frequency moments can be directly obtained from the $\tau = 0$ points. The first moment can be accurately extracted this way. In the case of the second moment the statistical fluctuations grow large as $\tau \rightarrow 0$, but the extrapolation provided by the Max-Ent fit still gives a quite stable result. We also extract the third moment from the Max-Ent spectra. For both $L = 4$ and $L = 6$ the results are in excellent agreement with the exact results obtained with the Lanczös method in Sec. III.

Fig. 8 shows the system size dependence of both the QMC and the Lanczös results for the cumulants, along with the previous²² infinite-size series results by Singh *et al.*. We also include the first and second cumulants obtained for a 16×16 lattice, for which we do not consider the full line shape obtained with the Max-Ent method to be stable due to larger statistical errors than for the smaller systems. The first two cumulants can nevertheless be estimated. The Max-Ent and series results agree very well for the larger systems. The exact results for the non-square lattices do not show a regular size dependence, whereas the $L \times L$ lattices do. The *moments* for the $L \times L$ lattices increase monotonically with L . However, there is a clear maximum in the second cumulant for $L = 6$. This is likely caused by the lack of weight between the two dominant peaks for this lattice size. With growing size the gap should gradually be filled in by other peaks, leading to a decreasing second cumulant. Judging from Fig. 8, the results for the largest systems (16×16 for M_1 and M_2 and 10×10 for M_3) should represent the thermodynamic limit within statistical errors. We then have $M_1 = 3.59 \pm 0.01$, $M_2 = 0.79 \pm 0.03$, and $M_3 = 0.95 \pm 0.08$.

We now return to the line shape. The Max-Ent spectra displayed in Fig. 6 show a considerable dependence on the lattice size. The trend for $L \geq 6$ appears to be the development of a well defined main peak at $\omega/J \approx 3.5$, as well as some strengthening of the tail up to $\omega/J \approx 7$. Comparing with the spinwave results for the two-magnon profiles shown in Fig. 2, the 10×10 Max-Ent spectrum is clearly much broader than the narrow peak obtained by Canali and Girvin,¹⁷ but not quite as much broadened towards lower frequencies as the Chubukov-Frenkel profile²⁴ obtained by setting $S = 1/2$ at a later stage of the calculation. Since the Max-Ent method can be expected to cause some broadening and the trend with increasing the lattice size appears to be a narrowing of the dominant peak, we conclude that the actual peak in the thermodynamic limit should be narrower than that obtained by Chubukov and Frenkel.

In the exact 6×6 result there are contributions in the frequency range $\omega/J \approx 4.5 - 7$ which are not present in the spinwave result for the same lattice (see Fig. 3). This

weight is therefore most likely dominated by processes involving more than two magnons. The Max-Ent result for the 10×10 lattice also shows a tail extending up to $\omega/J \approx 7$. The total weight above the spinwave theory two-magnon cut-off $\omega/J = 4.63$ does, however, remain at $\approx 10 - 15\%$, as previously argued on the basis of the $1/S^2$ spinwave results and the frequency cumulants.¹⁷

Canali and Girvin argued that the two-magnon profile is very little affected by the higher-order processes, and that the four-magnon contribution should be a peak well separated from the two-magnon profile.¹⁷ We now consider an approach to testing this hypothesis numerically, independently of the Max-Ent method. We assume a spectrum consisting of the Canali-Girvin two-magnon profile $P(\omega)$ shown in Fig. 2, and a Gaussian $G_{\sigma_4}(\omega - \omega_4)$ of width σ_4 centered at $\omega = \omega_4$ for modeling the higher-order contribution. In order to account for a possible further frequency shift, we use a phenomenological frequency renormalization Z in the two-magnon profile. The full spectrum is hence

$$I(\omega) = A_2 P(Z\omega) + A_4 G_{\sigma_4}(\omega - \omega_4), \quad (31)$$

where P and G_{σ_4} are both normalized to one, and hence $A_2 + A_4 = 1$. We then have four parameters; Z , A_4 , ω_4 , and σ_4 which can be adjusted to give the best consistency with the imaginary-time data. Note that $P(\omega)$ already contains the spinwave renormalization factor to order $1/S^2$, and hence our Z should be close to 1 for this treatment to be consistent.

For the 10×10 lattice, the imaginary-time data can indeed be very well accounted for by this spectrum. We obtain the parameters $Z = 0.97$, $A_4 = 0.40$, $\omega_4 = 4.1$ and $\sigma_4 = 1.1$. The resulting spectrum is shown in Fig. 9. The data for 16×16 spins can also be very well fit to the form considered, and the parameters are not changed much from the 10×10 ones. This spectrum is also shown in Fig. 9. The parameters of the Gaussian are such that it is completely merged with the two-magnon profile. This is clearly consistent with both the 6×6 Lanczös and the Max-Ent results, which did not show any significant gap between the main peak and the high-frequency weight. In Fig. 9 the weight of the Gaussian also extends to the low-frequency side of the two-magnon peak, and therefore has the effect of broadening it. Therefore, the relative weight of about 40% of the secondary peak cannot be interpreted directly as the total four-magnon (and higher) contribution, but also likely reflects that the two-magnon profile from spinwave theory is too narrow. We have also carried out fits to two Gaussians, and then find that the dominant one is at a position $\approx 3.2J$, and the second one again is at $\approx 4 - 4.5J$. However, the uncertainty in the width of the dominant peak is large, and therefore this method cannot be used to accurately determine the width. Based on the other approaches we have discussed, we can nevertheless conclude that the standard spinwave two-magnon profile is too narrow, but by how much is not completely clear. The profile shown in Fig. 9 likely represents a lower bound of the width.

We also attempted a similar fitting procedure using the Chubukov-Frenkel two-magnon result as the dominant feature. However, we found that it was not possible to obtain any good fit to the QMC data in this case, due to the, apparently, too high low-energy weight.

In Fig. 9 we also show an experimental spectrum for La_2CuO_4 , with the frequency scale adjusted to give the same peak position $\omega/J \approx 3.25$ as the QMC-spinwave fit. This peak position corresponds to an exchange constant $J = 1440$ K for the experimental system, which is in good agreement with $J \approx 1500$ K obtained from Neutron scattering and NMR experiments. Although the experimental spectrum is somewhat broader than our result, there is a quite good agreement with the distribution of the weight present above the two-magnon cut-off frequency. Since the width of the theoretical spectrum shown here most probably is a lower bound of the actual width, we do not consider the deviations from the experimental spectrum serious. Comparing with the two-magnon spinwave spectra shown in Fig. 2, it is clear that our present fitted spectrum is considerably closer to the experimental result. As will be discussed further in Sec. VI, the width of the peak is such that the further broadening required to match the experimental spectrum could quite easily be achieved by spin-phonon couplings, as has been suggested by several groups.

V. FINITE-TEMPERATURE RESULTS

In this section we present results of QMC and Max-Ent calculations carried out at temperatures $T/J = 0.25$, 0.5 , and 1.0 .⁴⁵ Raman spectra for a 4×4 lattice at these temperatures were previously obtained by Bacci and Gagliano using exact diagonalization.³⁰ Recently, finite temperature Lanczös calculations for lattices with up to 20 sites were presented by Prelovšek and Jaklič.⁴⁶ Here we compare QMC+Max-Ent results for systems with 4×4 and 16×16 spins. The latter size should be sufficient for obtaining thermodynamic limit results at the temperatures considered.

Fig. 10 shows the imaginary-time correlation functions. For the temperatures considered here, $g(\tau)$ can be accurately evaluated for the whole range $0 \leq \tau \leq \beta$. The slower decay with τ for the larger lattice indicates the presence of more low-frequency weight as the system size increases. This is confirmed by the Max-Ent results for the real-frequency spectra, shown in Fig. 11. The results for 4×4 spins are in reasonable agreement with exact diagonalization results if one includes some rather large broadening of the δ -functions. In Fig. 11 we have graphed the exact results as histograms, with the bin width for each temperature chosen large enough to remove most, but not all, of the jagged structure due to the discrete finite-size spectrum. It is clear that the Max-Ent method cannot capture the fine-structure of the spectrum, and instead gives a single rounded shape. Nevertheless, the

region of dominant spectral weight and its temperature variations are well reproduced. The low-frequency peak in the exact 4×4 spectra at high temperatures is due to degeneracies present for this small lattice³⁰ (i.e., the peak is actually at $\omega = 0$).

Our 16×16 results show a faster enhancement of the low-frequency spectral weight as the temperature is increased above $T/J \approx 0.25$. This difference between lattice sizes is likely due to the presence of large finite-size gaps in the level spectrum of the 4×4 system. Naturally, as $T \rightarrow \infty$ the system size dependence should diminish, and this is seen already at $T = 1.0$ in Fig. 11. The finite-temperature spectra calculated for 20 sites by Prelovšek and Jaklič⁴⁶ for $T/J = 1.0$ and 0.5 are in reasonable agreement with our 16×16 results, again taking into account a Max-Ent broadening of our spectra. However, at $T/J = 0.5$, judging from the rather large differences between the exact results for $N = 16$ (Ref. 30) and $N = 20$ (Ref. 46) and the slow approach to the thermodynamic limit discussed in sec. IV, it is likely that the $N = 20$ spectrum has not yet converged to its infinite-size shape. The actual width at this temperature should therefore be something intermediate between our 16×16 Max-Ent result and the previously obtained $N = 20$ profile.

Experimentally, spectra taken at room temperature do not differ significantly from ones obtained at very low temperatures.^{13,14} As the temperature is elevated to $T/J \approx 0.5$ there is a significant increase in the weight below $\omega \approx 2J$.¹⁴ This feature is indeed quite well reproduced by our result for 16×16 spins.

The spectra shown in Fig. 11 are all normalized to 1. The temperature dependence of the integrated intensity is a quantity of experimental interest. We define two intensities:

$$I_1 = \int_{-\infty}^{\infty} d\omega A(\omega), \quad (32a)$$

$$I_2 = \int_0^{\infty} d\omega A(\omega). \quad (32b)$$

These definitions are equivalent at $T = 0$, but differ at finite T due to spectral weight at negative frequencies, with $A(-\omega) = e^{-\beta\omega} A(\omega)$. I_1 can be directly obtained from the imaginary-time data as $G(\tau = 0)$, whereas I_2 is calculated by integrating the real frequency spectrum obtained using the ME method. Fig. 12 shows both intensities vs. T for 4×4 and 16×16 lattices. Up to $T/J \approx 0.25$, $I_1 \approx I_2$, owing to the absence of significant low-frequency weight at these temperatures. At higher temperatures $I_1 > I_2$, but even at $T/J \approx 0.5$ the difference is small. For the 4×4 system the intensity I_2 increases by $\approx 14\%$ as the temperature is decreased from $T/J = 0.5$ to $T/J = 0$, and for 16×16 by $\approx 9\%$.

VI. SUMMARY AND DISCUSSION

We have presented numerical results for the B_{1g} spectrum of the Heisenberg model within Loudon-Fleury theory. We obtained Lancz s exact diagonalization results for up to 6×6 spins, and carried out QMC simulations for up to 16×16 spins. We compared the results with spin wave theory. Our main results and conclusions are the following:

1) Comparing spinwave theory and exact diagonalization results for the same lattice sizes, we find that for a given cluster the number of dominant peaks is the same in both cases. However, both the positions of the peaks and their relative weights are different. Most notably, for the 6×6 lattice there are two dominant peaks, the separation of which is 1.5 times larger in the exact result. Assuming that the trend persists for larger lattices, this indicates that spinwave theory underestimates the width of the dominant B_{1g} peak in the thermodynamic limit.

2) Our results of Maximum-Entropy analytic continuation of QMC imaginary-time data is also consistent with a peak width larger than that of the spinwave two-magnon peak. The first three frequency cumulants are in excellent agreement with previous results of a series expansion around the Ising model. We estimate the cumulants in the thermodynamic limit to be $M_1 = 3.59 \pm 0.01$, $M_2 = 0.79 \pm 0.03$, and $M_3 = 0.95 \pm 0.08$.

3) In order to test the $1/S^2$ spinwave theory prediction of a four-magnon profile well separated from the main two-magnon peak,¹⁷ we carried out a fit of the QMC imaginary-time data to a spectrum consisting of the spinwave two-magnon peak and a Gaussian at higher frequency. We found that this type of spectrum indeed describes the data well. The fitted Gaussian is centered at $\omega/J \approx 4.1$, and is so broad that it is completely merged together with the two-magnon structure peaked at $\omega/J \approx 3.25$. The resulting spectrum resembles a typical experimental B_{1g} profile for La_2CuO_3 with an exchange $J \approx 1400$ K. The experimental peak is still slightly broader, but there is a considerable improvement in comparison with the standard spinwave theory two-magnon profile.

4) The imaginary-time data cannot be fitted using the two-magnon profile obtained by Chubukov and Frenkel²⁴ by expanding their spinwave spectrum around its peak position before setting $S = 1/2$ in the calculation. This is due to the significantly stronger low-frequency weight present in this spectrum.

5) At finite temperature we find a significant increase in spectral weight below $\omega \approx 2J$ for $T/J \gtrsim 0.25$, in agreement with experimental results for antiferromagnetic cuprates.¹⁴ We also find that this effect is suppressed in the 4×4 system, due to the finite-size gaps. The temperature dependence of the integrated scattering intensity is weak.

Our results hence confirm that LF theory can account for some of the main features of typical B_{1g} spectra

observed experimentally for antiferromagnetic cuprates such as La_2CuO_4 . Our new evidence for a profile significantly broader than that obtained in spinwave theory support in part the early claim by Singh *et al.*²² that the broadening is due to the strong quantum fluctuations of the Heisenberg model with $S = 1/2$ (note that spinwave theory is in good agreement with experimental results for quasi-2D $S = 1$ systems⁴⁷). However, typical experimental spectra are still broader, and extend to slightly higher frequencies. The shoulder-like feature observed in some experiments at $\omega \approx 4J$ is also not present in our results, although we find evidence that the four-magnon contribution has its maximum in this regime. Hence, although our results show a better agreement with experiments than previous numerical results obtained for smaller lattices,^{19,30} the Heisenberg-LF mechanism does not appear to fully account for the experimental Raman scattering, as has been noted in several previous studies. The fact that there is no A_{1g} scattering within this theory of course also implies that other additional mechanisms have to be active.

Chubukov and Frenkel recently suggested that resonant processes not contained within LF theory are important in typical experiments, for which the frequency ω_{in} of the incident light is comparable to the charge transfer gap of the CuO_2 planes.²⁴ We agree that resonance effects are most likely needed to explain the dependence of the total scattering intensity and the line shape on ω_{in} ,¹⁵ but note that the dominant features of the profile do not show much dependence on ω_{in} for most of the frequencies studied.^{13,15} Based on the improved agreement with experiments obtained here within LF theory, we believe that the main features of the B_{1g} spectrum are due to the LF mechanism, and that a further broadening of the spectrum could be achieved by magnon damping due to phonons.

Motivated by experiments carried out at high temperatures, Knoll *et al.* suggested that spin-lattice interactions may be responsible for the broadening of the Raman spectrum.¹⁴ Spinwave calculations including a phenomenological magnon life-time give some support to these ideas.³¹ Several different calculations explicitly including magnon-phonon coupling have been presented recently.^{32,33,34} Using an adiabatic approximation for the phonons leads to a Heisenberg model with random coupling constants. Numerically studying such random lattices with 4×4 spins and assuming a standard LF coupling, Nori *et al.* found that the B_{1g} spectrum can indeed be broadened by this mechanism, and that also A_{1g} scattering can become significant.³² However, in this calculation, the strength of the randomness required in order to reproduce the width of the experimental B_{1g} spectrum appears to be rather large (using a Gaussian distribution for the nearest-neighbor couplings J_{ij} , a width $\sigma \approx 0.5\langle J_{ij} \rangle$ was required).⁴⁸ Nori *et al.* argued that such strong disorder can be caused by incoherent atomic displacements. Nevertheless, in the absence of other evidence for the presence of large fluctuations in the Heisen-

berg couplings, it would be desirable to reproduce the broadened spectrum with a narrower coupling distribution.

One reason for the strong disorder required in the calculation of Nori *et al.* could be the small size of the lattice used.³² As we have seen, the pure 4×4 system only has a single dominant two-magnon δ -function at $\omega = 2.98J$, and two weaker peaks at $\omega \approx 4.5J$ and $\omega \approx 5.5J$.¹⁹ It is clear that a considerably weaker disorder would suffice to broaden the spectrum if one starts from the much broader pure-system profile obtained here for larger lattices.

The type of QMC and Max-Ent calculations presented here could in principle be carried out also for disordered spin systems, and even including fully dynamic phonons.⁴⁹ The suggested effects of magnon-phonon coupling could hence be investigated more rigorously than previously, using larger lattices. Although a recent exact diagonalization study by Reilly and Rojo⁵⁰ give some support for the validity of an adiabatic approximation for the phonons, calculations with full dynamic phonons should also be carried out for larger lattices. Limits on the strength of the phonon-magnon coupling (or the width of the disorder distribution in the adiabatic approach) could be established by carrying out QMC calculations of, e.g., the temperature dependence of the spin correlation length⁸ and NMR relaxation rates¹² for systems including lattice vibrations or static disorder.

ACKNOWLEDGMENTS

We would like to thank G. Blumberg, C. Canali, A. Chubukov, S. Girvin, D. Morr, R. Singh, and P. Prelovšek for useful discussions and correspondence. This work was supported by the National Science Foundation under Grants No. DMR-95-20776, DMR-95-27304 and -DMR-97-12765. The QMC calculations were carried out at the Supercomputer Computations Research Institute at Florida State University.

APPENDIX A: QMC CALCULATIONS OF THE RAMAN CORRELATION FUNCTIONS

In this Appendix we describe the calculation of the imaginary-time correlation function (22) with the stochastic series expansion (SSE) method.^{27,28} In order to reduce the statistical fluctuations, we use the spin-rotational invariance of the Heisenberg Hamiltonian to construct an estimator less noisy than the obvious one. We also derive direct estimators for the τ -derivatives of $G(\tau)$. In order to establish the notation, we first very briefly outline the formalism of the SSE algorithm. More details of the implementation of this non-standard generalization of Handscomb's method^{51,52} for the 2D Heisenberg model can be found in Ref. 29.

In order to apply the SSE technique, the Hamiltonian is first written as

$$\hat{H} = -\frac{J}{2} \sum_{b=1}^{2N} [\hat{H}_{1,b} - \hat{H}_{2,b}] + \frac{NJ}{2}, \quad (\text{A1})$$

where b is a link connecting a pair of nearest-neighbor sites $\langle i(b), j(b) \rangle$, and the operators $\hat{H}_{1,b}$ and $\hat{H}_{2,b}$ are defined as

$$\hat{H}_{1,b} = 2[\frac{1}{4} - S_{i(b)}^z S_{j(b)}^z] \quad (\text{A2a})$$

$$\hat{H}_{2,b} = S_{i(b)}^+ S_{j(b)}^- + S_{i(b)}^- S_{j(b)}^+. \quad (\text{A2b})$$

An exact expression for an operator expectation value

$$\langle \hat{A} \rangle = \frac{1}{Z} \text{Tr}\{\hat{A} e^{-\beta \hat{H}}\}, \quad Z = \text{Tr}\{e^{-\beta \hat{H}}\}, \quad (\text{A3})$$

at inverse temperature $\beta = J/T$, is obtained by Taylor expanding $\exp(-\beta \hat{H})$ and writing the traces as sums over diagonal matrix elements in the basis $\{|\alpha\rangle\} = \{|S_1^z, \dots, S_N^z\rangle\}$. The partition function then takes the form²⁷

$$Z = \sum_{\alpha} \sum_n \sum_{S_n} \frac{(-1)^{n_2}}{n!} \left(\frac{\beta}{2}\right)^n \langle \alpha | \prod_{l=1}^n \hat{H}_{a_l, b_l} | \alpha \rangle, \quad (\text{A4})$$

where S_n is a sequence of index pairs defining the operator string $\prod_{l=1}^n \hat{H}_{a_l, b_l}$,

$$S_n = [a_1, b_1][a_2, b_2] \dots [a_n, b_n], \quad (\text{A5})$$

with $a_i \in \{1, 2\}$, $b_i \in \{1, \dots, 2N\}$, and n_2 denotes the total number of index pairs (operators) $[a_i, b_i]$ with $a_i = 2$. Both $\hat{H}_{1,b}$ and $\hat{H}_{2,b}$ can act only on states where the spins at sites $i(b)$ and $j(b)$ are antiparallel. $\hat{H}_{1,b}$ leaves such a state unchanged, whereas $\hat{H}_{2,b}$ flips the spin pair. Defining a propagated state

$$|\alpha(p)\rangle = \prod_{l=1}^p \hat{H}_{a_l, b_l} |\alpha\rangle, \quad |\alpha(0)\rangle = |\alpha\rangle, \quad (\text{A6})$$

a contributing (α, S_n) must clearly satisfy the periodicity condition $|\alpha(n)\rangle = |\alpha(0)\rangle$. In an allowed sequence S_n , the links b corresponding to the spin-flipping operators $[2, b]$ present must therefore form only closed loops. For a lattice with $L \times L$ sites and L even, this implies that the number n_2 must be even, and hence that all terms in Eq. (A4) are positive and can be used as relative probabilities in a Monte Carlo algorithm (this is true for any non-frustrated system). Since any non-zero matrix element in (A4) is equal to one, the weight factor corresponding to a contributing (α, S_n) is simply given by

$$W(\alpha, S_n) = \frac{(\beta/2)^{n_2}}{n!}. \quad (\text{A7})$$

The algorithm for sampling the configurations (α, S_n) is described in Ref. 29.

In order to obtain an expression for $G(\tau)$ in terms of the states $|\alpha(p)\rangle$ and the index sequence S_n used in the simulation, the expectation value is first written in terms of the operators $\hat{H}_{a,b}$ as

$$G(\tau) = \sum_{a_1, a_2} \sum_{b_1, b_2} P_{b_1, b_2} G_{a_2, b_2}^{a_1, b_1}(\tau), \quad (\text{A8})$$

where

$$G_{a_2, b_2}^{a_1, b_1}(\tau) = \langle H_{a_2, b_2}(\tau) H_{a_1, b_1}(0) \rangle, \quad (\text{A9})$$

and B_{1g} symmetry corresponds to $P_{b_1, b_2} = 1$ for links b_1 and b_2 which are parallel to each other, and $P_{b_1, b_2} = -1$ for perpendicular links. Proceeding as in the derivation of the partition function (A4), the exponentials in the expression

$$G_{a_2, b_2}^{a_1, b_1}(\tau) = \frac{1}{Z} \sum_{\alpha} \langle \alpha | e^{-(\beta-\tau)\hat{H}} \hat{H}_{a_2, b_2} e^{-\tau\hat{H}} \hat{H}_{a_1, b_1} | \alpha \rangle \quad (\text{A10})$$

are Taylor expanded and all powers of \hat{H} are written as sums of products of the operators $\hat{H}_{a,b}$. There is then a one-to-one correspondence between the terms in $G_{a_2, b_2}^{a_1, b_1}(\tau)$ and Eq. (A4). Dividing out the factor corresponding to the configuration weight (A7) gives the average in the form of a function of S_n :

$$G_{a_2, b_2}^{a_1, b_1}(\tau) = \left\langle \sum_{m=0}^{n-2} F(\tau, n; m) N_{a_2, b_2}^{a_1, b_1}(m) \right\rangle, \quad (\text{A11})$$

where

$$F(\tau, n; m) = \frac{\tau^m (\beta - \tau)^{n-m-2} (n-1)!}{\beta^n (n-m-2)! m!}, \quad (\text{A12})$$

and $N_{a_2, b_2}^{a_1, b_1}(m)$ is the number of times the operators $[a_1, b_1]$ and $[a_2, b_2]$ occur in S_n (in the given order) separated by m other operators. Hence, measuring $G_{a_2, b_2}^{a_1, b_1}(\tau)$ simply amounts to finding all pairs of operators $[a_1, b_1]$ and $[a_2, b_2]$ in the sequence S_n . The contribution to Eq. (A10) of each pair is a function of the relative separation of the operators, given by Eq. (A12).

In order to obtain a simple expression for the full correlation function $G(\tau)$ it is useful to introduce a function $X(p)$, such that $X(p) = +1$ if the p :th operator in S_n acts on a link in the x -direction, and $X(p) = -1$ if it acts on a y link. Numbering the bonds such that $0 \leq b \leq N$ correspond x -bonds, and $N+1 \leq b \leq 2N$ correspond to y -bonds, the definition is hence

$$X(p) = \begin{cases} +1, & b_p \leq N \\ -1, & b_p > N. \end{cases} \quad (\text{A13})$$

Eqs. (A9) and (A11) then give

$$G(\tau) = \left\langle \sum_{p=1}^n \sum_{m=1}^{n-1} F(\tau, n, m-1) X(p) X(p+m) \right\rangle, \quad (\text{A14})$$

where of course $X(p)$ is periodic; $X(n+1) = X(1)$.

In practice the estimator (A14) is rather noisy. An improved estimator can be constructed as follows. First, the function $X(p)$ is written as a sum of two terms,

$$X(p) = X_1(p) + X_2(p), \quad (\text{A15})$$

where $X_t(p) = \pm 1$ ($t = 1, 2$) for x and y bonds, as before, if the p :th operator in S_n , $[a_p, b_p]$, has $a_p = t$, but $X_t(p) = 0$ if $a_p \neq t$. Hence

$$X_t(p) = \begin{cases} +1, & a_p = t, \quad b_p \leq N \\ -1, & a_p = t, \quad b_p > N \\ 0, & a_p \neq t \end{cases} \quad (\text{A16})$$

If $a_p = 1$, $X_1(p)$ can be averaged over all $2N$ choices of operators $[1, b]$ at position p . The weight $W(\alpha, S'_n)$ corresponding to a sequence S'_n obtained by replacing the current operator $[1, b_p]$ at p in S_n is equal to the current weight $W(\alpha, S_n)$ if the corresponding spins at sites $i(b)$ and $j(b)$ are antiparallel in the propagated state $|\alpha(p)\rangle$, and is zero otherwise. Hence, $X_1(p)$ can be redefined as

$$X_1(p) = \begin{cases} [N_x^A(p) - N_y^A(p)]/2N, & a_p = 1 \\ 0, & a_p \neq 1 \end{cases} \quad (\text{A17})$$

where $N_\gamma^A(p)$ is the number of antiparallel nearest-neighbor spin pairs in the γ -direction in $|\alpha(p)\rangle$. One can easily verify that this averaged estimator can be used in products with both X_1 and X_2 . Hence, improved estimators for $X(p)X(p+m)$ in Eq. (A14) can be used for the terms X_1X_1 , X_1X_2 , and X_2X_1 . For $X_2(p)$ no simple re-definition in terms of single-operator averaging can be constructed (replacing a single operator $[2, b]$ with any other operator always leads to a non-contributing term), and hence the X_2X_2 contribution to (A14) remains noisy. However, the rotational invariance of the Heisenberg Hamiltonian implies that,

$$\langle X_2(p) X_2(p+m) \rangle = \langle 2X_1(p) X_1(p+m) \rangle + \frac{1}{2} \langle X_1(p) X_2(p+m) + X_2(p) X_1(p+m) \rangle, \quad (\text{A18})$$

and therefore the X_2X_2 term does not even have to be evaluated. The final result for the improved estimator for $G(\tau)$ is hence

$$G(\tau) = \left\langle \frac{3}{2} \sum_{p=1}^n \sum_{m=1}^{n-1} F(\tau, n; m-1) \left[2X_1(p) X_1(p+m) + X_1(p) X_2(p+m) + X_2(p) X_1(p+m) \right] \right\rangle. \quad (\text{A19})$$

It should be noted that the function $F(\tau, n; m)$ is sharply peaked around $m \approx n\tau/\beta$ for large β , so that typically

only a small fraction of the terms in (A19) actually have to be evaluated.

Eq. (A19) is valid for any $0 \leq \tau \leq \beta$, and the τ -dependence appears only in the function $F(\tau, n; m)$. In contrast to standard Trotter-based QMC methods, the method discussed here can therefore be used to directly calculate also τ -derivatives of imaginary-time dependent correlation functions. An expression for the n :th derivative of $G(\tau)$ is simply obtained by replacing F in (A19) by its n :th derivative:

$$G^{(n)}(\tau) = \frac{d^n G(\tau)}{d\tau^n} = \left\langle \frac{3}{2} \sum_{p=1}^n \sum_{m=1}^{n-1} \times \left(\frac{d^n F(\tau, n, m-1)}{d\tau^n} \right) \left[2X_1(p)X_1(p+m) + X_1(p)X_2(p+m) + X_2(p)X_1(p+m) \right] \right\rangle. \quad (\text{A20})$$

As discussed in Sec. IV, derivatives can be used as supplementary information in a numerical analytic continuation to real frequency. The derivatives at $\tau = 0$ are of special interest, as they are related to moments of the spectral function [see Eq. (29)].

We end this Appendix with a demonstration that the simulation results for $G(\tau)$ are indeed free from systematic errors. Since the absolute Raman scattering intensity is not contained in the LF theory, the amplitude of $I(\omega)$, and hence of $G(\tau)$, is irrelevant, and instead of $G(\tau)$ one can consider the ratio

$$g(\tau) = G(\tau)/G(0). \quad (\text{A21})$$

Fig. 13 shows the QMC result for this quantity calculated on a 4×4 lattice, along with the exact result obtained from $I(\omega)$ calculated using exact diagonalization. The statistical error of the QMC result is in the fifth decimal digit, and there is excellent agreement with the exact result within this accuracy. The absence of detectable systematical errors in the QMC result for $g(\tau)$ is hence confirmed. Since $g(\tau)$ decays exponentially, the relative statistical error grows rapidly with τ , and for $\tau \gtrsim 3$ accurate results can not be easily obtained. This is the case also for larger systems.

¹ For a review, see E. Manousakis, Rev. Mod. Phys. **63**, 1 (1991).

² D. Vaknin *et al.*, Phys. Rev. Lett. **58**, 2802 (1987); G. Shirane *et al.*, Phys. Rev. Lett. **59**, 1613 (1987); Y. Endoh *et al.*, Phys. Rev. B **37**, 7443 (1988).

³ G. Aeppli *et al.*, Phys. Rev. Lett. **62**, 2052 (1989); S. M. Hayden *et al.*, Phys. Rev. B **42**, 10220 (1990); S. M. Hayden *et al.*, Phys. Rev. Lett. **67**, 3622 (1991).

⁴ P. Bourges, H. Casalta, A. S. Ivanov, and D. Petitgrand, preprint, cond-mat/9708060 (1997).

⁵ T. Imai *et al.* Phys. Rev. Lett. **70**, 1002 (1993); *ibid.*, **71**, 1254 (1993).

⁶ M. Matsumura *et al.*, J. Phys. Soc. Jpn **63**, 4331 (1994).

⁷ S. Chakravarty, B. I. Halperin, and D. R. Nelson, Phys. Rev. Lett. **60**, 1057 (1988); Phys. Rev. B **39**, 2344 (1989).

⁸ H.-Q. Ding and M. S. Makivić, Phys. Rev. Lett. **64**, 1449 (1990); M. S. Makivić and H.-Q. Ding, Phys. Rev. B **43**, 3562 (1991).

⁹ M. Makivić and M. Jarrell, Phys. Rev. Lett. **68**, 1770 (1992).

¹⁰ S. Sachdev and J. Ye, Phys. Rev. Lett. **69** 2411 (1992); A. V. Chubukov and S. Sachdev, Phys. Rev. Lett. **71**, 169 (1993); A. V. Chubukov, S. Sachdev, and J. Ye, Phys. Rev. B **49**, 11919 (1994).

¹¹ A. Sokol, E. Gagliano, and S. Bacci, Phys. Rev. B **47**, 14646 (1993); A. Sokol, R.L. Glenister, and R.R.P. Singh, Phys. Rev. Lett. **72**, 1549 (1994).

¹² A. W. Sandvik and D. J. Scalapino, Phys. Rev. B **51**, 9403 (1995).

¹³ K. B. Lyons *et al.*, Phys. Rev. B **39**, 2293 (1989); I. Ohana *et al.*, *ibid.* **39**, 2293 (1989); P. E. Sulewski *et al.*, *ibid.* **41**, 225 (1990); S. Sugai *et al.*, *ibid.*, **42**, 1045 (1990);

¹⁴ P. Knoll *et al.*, Phys. Rev. B **42**, 4842 (1990).

¹⁵ G. Blumberg *et al.*, Phys. Rev. B **53**, 11930 (1996).

¹⁶ J. B. Parkinson, J. Phys. C **2**, 2012 (1969).

¹⁷ C. M. Canali and S. M. Girvin, Phys. Rev. B **45**, 7127 (1992).

¹⁸ M. Roger, J. M. Delrieu, Phys. Rev. B. **39**, 2299 (1989).

¹⁹ S. Chakravarty, in *Proceedings of the Los Alamos Symposium 1989, High Temperature Superconductivity*, edited by K. S. Bedell *et al.* (Addison-Wesley, Reading MA, 1990); E. Gagliano and S. Bacci, Phys. Rev. B **42**, 8772 (1990); E. Dagotto and D. Poilblanc, *ibid.*, **42**, 7940 (1990); F. Nori, E. Gagliano, and S. Bacci, Phys. Rev. Lett. **68**, 240 (1992).

²⁰ P. A. Fleury and R. Loudon, Phys. Rev. **166**, 514 (1968).

²¹ B. S. Shastry and B. I. Shraiman, Phys. Rev. Lett. **65**, 1068 (1990); Int. J. Mod. Phys. B **5**, 365 (1991).

²² R. R. P. Singh, P. A. Fleury, K. B. Lyons, and P. E. Sulewski, Phys. Rev. Lett. **62**, 2736 (1989).

²³ Y. Honda, Y. Kuramoto, and T. Watanabe, Physica C **185-189**, 1493 (1991); Phys. Rev. B **47**, 11329 (1993).

²⁴ A. V. Chubukov and D. M. Frenkel, Phys. Rev. B **52**, 9760 (1995).

²⁵ R. R. P. Singh, P. Prelovšek, and B. S. Shastry, Phys. Rev. Lett. **77**, 4086 (1996).

²⁶ C. Gros *et al.*, Phys. Rev. B **55**, 15048 (1996).

²⁷ A. W. Sandvik and J. Kurkijärvi, Phys. Rev. B **43**, 5950 (1991).

²⁸ A. W. Sandvik, J. Phys. A **25**, 3667 (1992).

²⁹ A. W. Sandvik, Phys. Rev. B, to appear, Nov. 1 1997.

³⁰ S. Bacci and E. Gagliano, Phys. Rev. B **43**, 6224 (1991).

³¹ W. H. Weber and G. W. Ford, Phys. Rev. B **40**, 6890 (1989).

³² F. Nori *et al.*, Phys. Rev. Lett. **75**, 553 (1995).

³³ S. Manning and F. V. Kusmartsev, J. Phys. Soc. Jpn **64**, 2245 (1995).

³⁴ D. U. Saenger, Phys. Rev. B **49**, 12176 (1994); **52**, 1025 (1995).

- ³⁵ F. J. Dyson, Phys. Rev. **102**, 1217 (1956); **102**, 1230 (1956).
- ³⁶ S. V. Maleev, Zh. Eksp. Theor. Fiz. **30**, 1010 (1957) [Sov. Phys. JETP **64**, 654 (1958)].
- ³⁷ R. J. Elliott *et al.*, Phys. Rev. Lett. **21**, 147 (1968).
- ³⁸ T. Oguchi, Phys. Rev. **117**, 117 (1960).
- ³⁹ R. R. P. Singh, Phys. Rev. B **39**, 9760 (1989); B. B. Beard and U.-J. Wiese, Phys. Rev. Lett. **77**, 5130 (1996).
- ⁴⁰ R. N. Silver, D. S. Sivia, and J. E. Gubernatis, Phys. Rev. B **41**, 2380 (1990); J. E. Gubernatis, M. Jarrell, R. N. Silver, and D. S. Sivia, *ibid.*, B **44** (1991) 6011.
- ⁴¹ M. Jarrell and J. E. Gubernatis, Phys. Rep. **269**, 133 (1996).
- ⁴² H.-B. Schüttler and D. J. Scalapino, Phys. Rev. Lett. **55**, 1204 (1985); Phys. Rev. B **34**, 4744 (1986).
- ⁴³ S. R. White, Phys. Rev. B **44**, 4670 (1991).
- ⁴⁴ B. Efron and G. Gong, Am. Stat. **37**, 36 (1983).
- ⁴⁵ In Ref. 32 some initial finite-temperature QMC results were also presented. In these calculations the improved estimator introduced here (see Appendix A) for $G(\tau)$ was not used, and the accuracy was therefore not as high as in the results presented here.
- ⁴⁶ P. Prelovšek and J. Jaklič, Phys. Rev. B **53**, 15095 (1996).
- ⁴⁷ P. A. Fleury and H. J. Guggenheim, Phys. Rev. Lett. **24**, 1346 (1970).
- ⁴⁸ The comparison with the experimental spectrum presented in Ref 32 (the same one, from Ref. 22, as used here for comparison in Fig. 9) is slightly affected by an accidental shift of the zero point of the frequency axis. With the correct zero point, the estimate for the strength of the disorder required decreases by $\approx 15 - 20\%$.
- ⁴⁹ A. W. Sandvik, R. R. P. Singh, and D. K. Campbell, to appear in Phys. Rev. B (Nov. 1 1997).
- ⁵⁰ M. J. Reilly and A. G. Rojo, Phys. Rev. B **53**, 6429 (1996).
- ⁵¹ D. C. Handscomb, Proc. Cambridge Philos. Soc. **58**, 594 (1962); **60**, 116 (1964).
- ⁵² D. H. Lee, J. D. Joannopoulos, and J. W. Negele, Phys. Rev. B **30**, 1599 (1984).
- ⁵³ In practice, it is useful to explicitly truncate the expansion at some maximum $n = n_{\max}$, large enough to introduce no detectable systematical errors. One can then formulate a configuration space where the index sequence has a fixed length, by augmenting sequences shorter than n_{\max} by unit operators. This facilitates the construction of a fast updating algorithm. See Refs. 27 and 29.
- ⁵⁴ Scaling as βN , the index sequence is typically quite long at low temperatures. For example, for a 10×10 lattice at inverse temperature $\beta = 80$, the average length $\langle n \rangle \approx 9500$. However, only one of the states $|\alpha(p)\rangle$ has to be stored. The memory requirements are therefore significantly smaller than for standard Trotter based methods.

FIG. 1. Spinwave theory results for the B_{1g} Raman profile calculated on small lattices with $L \times L$ sites. The dashed curves are the results with the interactions neglected, and the solid ones are with interactions in the final states included at the RPA level. A damping $\epsilon = 0.05J$ has been used to broaden the δ -functions.

FIG. 2. Spinwave theory results for the B_{1g} two-magnon profile in the thermodynamic limit, compared with the experimental spectrum for La_2CuO_4 discussed in Ref. 22 (bold solid curve). The solid curve corresponds to Eq. (18) with a spinwave renormalization factor $Z_c = 1.158$. The dotted curve is the result by Canali and Girvin, which includes also quantum fluctuations in the ground state. The dashed line is the result by Chubukov and Frenkel, obtained by further expanding the line shape (18) in $1/S$ before setting $S = 1/2$. All curves are normalized to one. The frequency scale of the experimental spectrum has been adjusted to give a peak position in rough agreement with the theoretical curves.

FIG. 3. Exact diagonalization results for the B_{1g} spectrum for different small lattices with N sites (solid curves). The dashed curves are the corresponding RPA-spinwave results. The δ -functions of the exact results have been broadened using a damping $\epsilon = 0.1J$, and all the spectra are normalized to one. The spinwave results have been given a smaller damping and a different normalization in order to more clearly show the peak positions.

FIG. 4. QMC results for $\ln[g(\tau)]$ (upper panel) for different system sizes, and the relative statistical errors of $g(\tau)$ (lower panel).

FIG. 5. Results of Max-Ent analytic continuation of 10 bootstrap samples of QMC imaginary-time data generated for a 4×4 system.

FIG. 6. Bootstrap-averaged Max-Ent results for the B_{1g} spectrum for different lattices (solid curves). The 4×4 and 6×6 results are compared with the corresponding exact diagonalization results with a damping $\epsilon/J = 0.1$ (dotted curves).

FIG. 7. QMC results for the short-time behavior of $G^{(1)}/G$ (upper panel) and $G^{(2)}/G$ (lower panel) for systems of linear sizes $L = 4$ (solid circle), 6 (open circles), 8 (solid squares), and 10 (open squares). The solid curves are obtained from the Max-Ent analytic continuation.

FIG. 8. The first three frequency cumulants of the Max-Ent spectra vs. the inverse system size (solid circles with error bars). The open circles are the exact diagonalization results. The previous infinite-size results from a series expansion, calculated by Singh *et al.*,²² are indicated by the horizontal dashed lines (result \pm estimated error).

FIG. 9. B_{1g} spectrum obtained by a fit of imaginary-time QMC data to the Canali-Girvin two-magnon profile¹⁷ plus a Gaussian. The almost indistinguishable solid and dashed curves are for a 10×10 and a 16×16 lattice, respectively. The bold curve is the experimental spectrum for La_2CuO_4 discussed in Ref. 22, with the frequency scale adjusted to give the same peak position as the theoretical results (corresponding to an exchange $J = 1440$ K).

FIG. 10. The logarithm of the normalized imaginary-time correlator $g(\tau)$ vs. τ for 4×4 (dashed curves) and 16×16 (solid curves) lattices at different temperatures.

FIG. 11. Max-Ent results for the B_{1g} spectrum of 4×4 (dashed curves) and 16×16 (solid curves) lattices at different temperatures. The histograms represent the exact results for the 4×4 lattice.

FIG. 12. Integrated B_{1g} scattering intensities vs. temperature for 4×4 (open symbols) and 10×10 (solid symbols) lattices. Circles are for I_1 (using all frequencies), and squares for I_2 (using positive frequencies only).

FIG. 13. Upper panel: QMC results for $g(\tau) = G(\tau)/G(0)$ of a 4×4 system at inverse temperature $\beta = 32$ (solid circles), compared with the exact ground state result (solid curve). The inset shows the regime $1.75 \leq \tau \leq 3$ on a more detailed scale. Lower panel: The deviation of the QMC data from the exact result, multiplied by 10^4 . The dashed curves indicate the statistical errors.

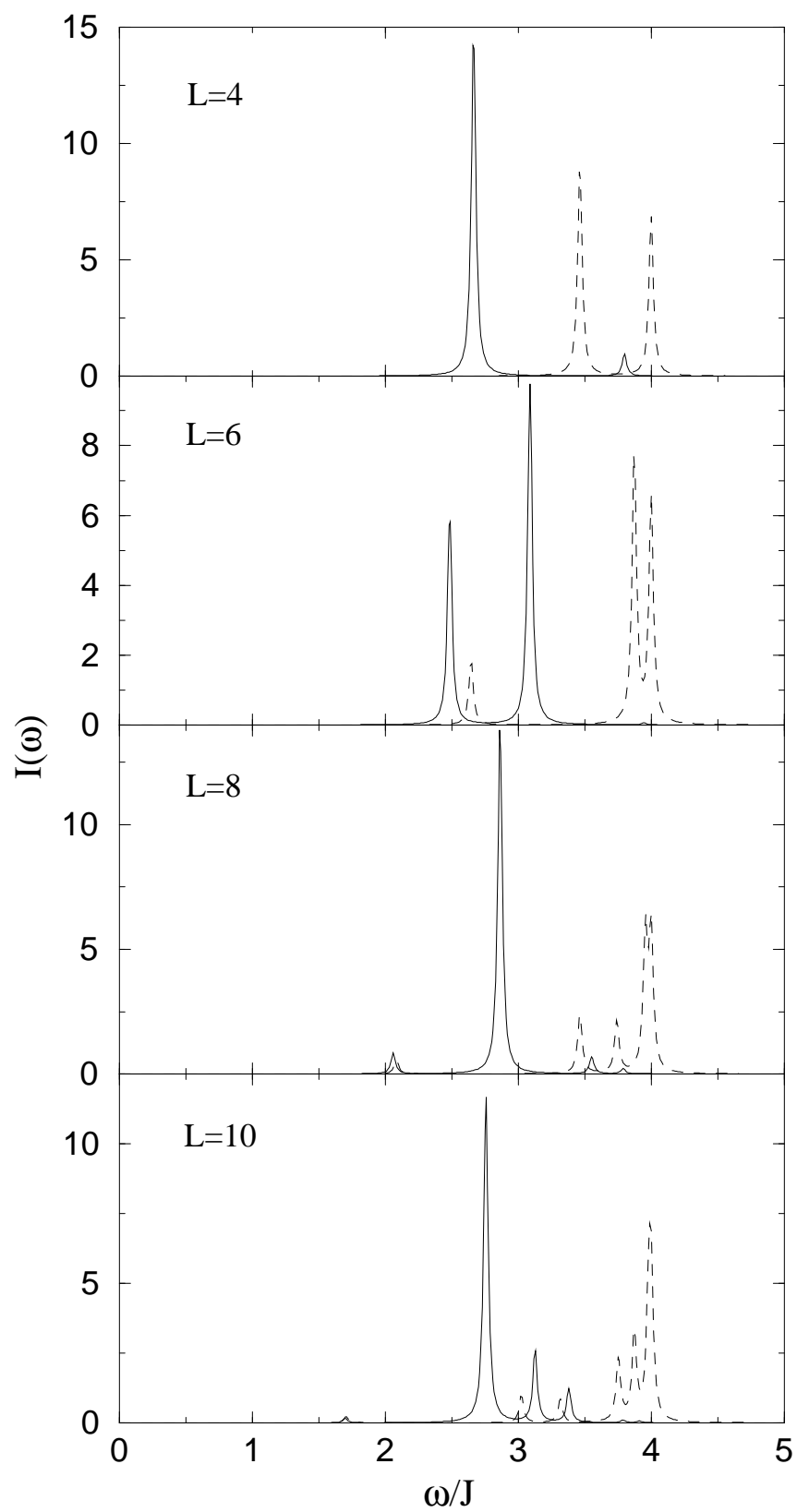


Fig. 1, A. W. Sandvik et al.

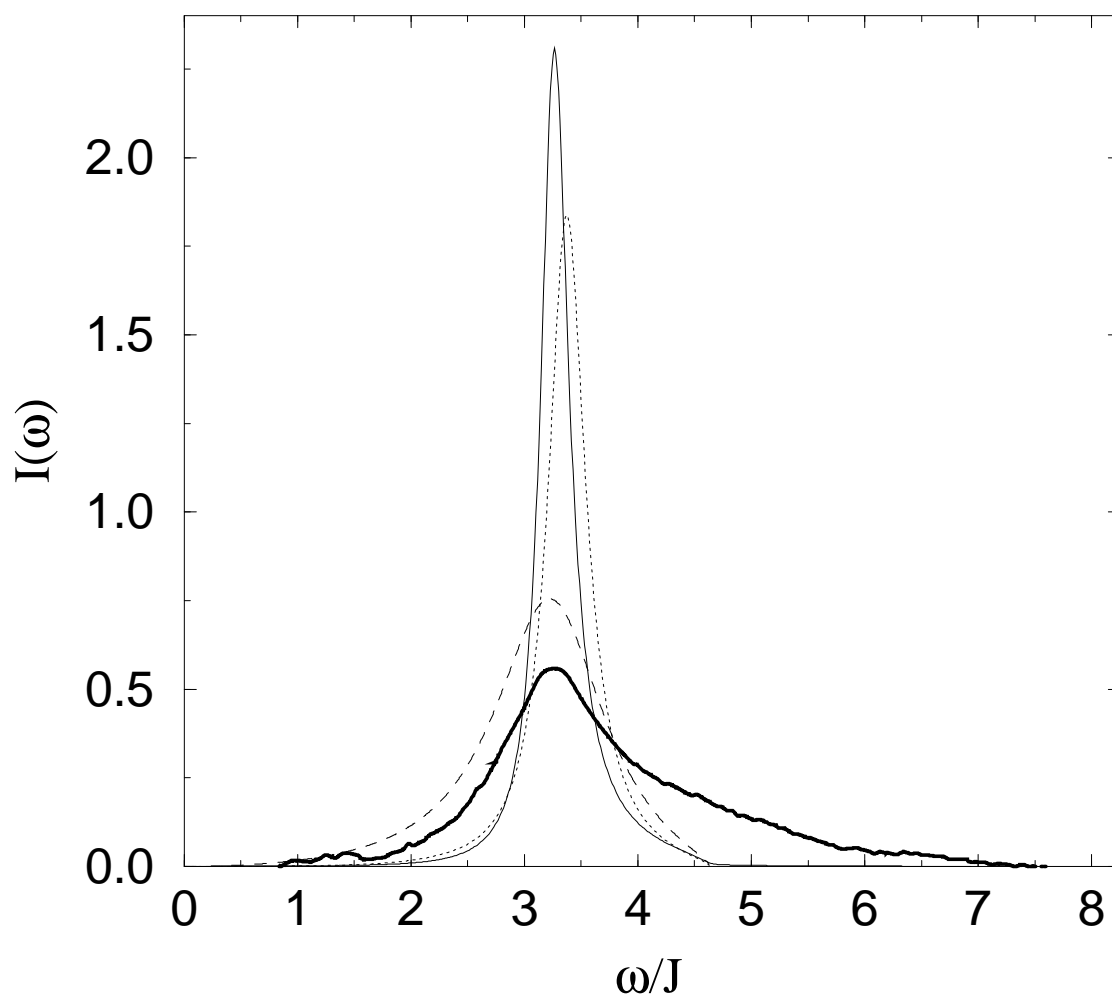


Fig. 2, A. W. Sandvik et al.

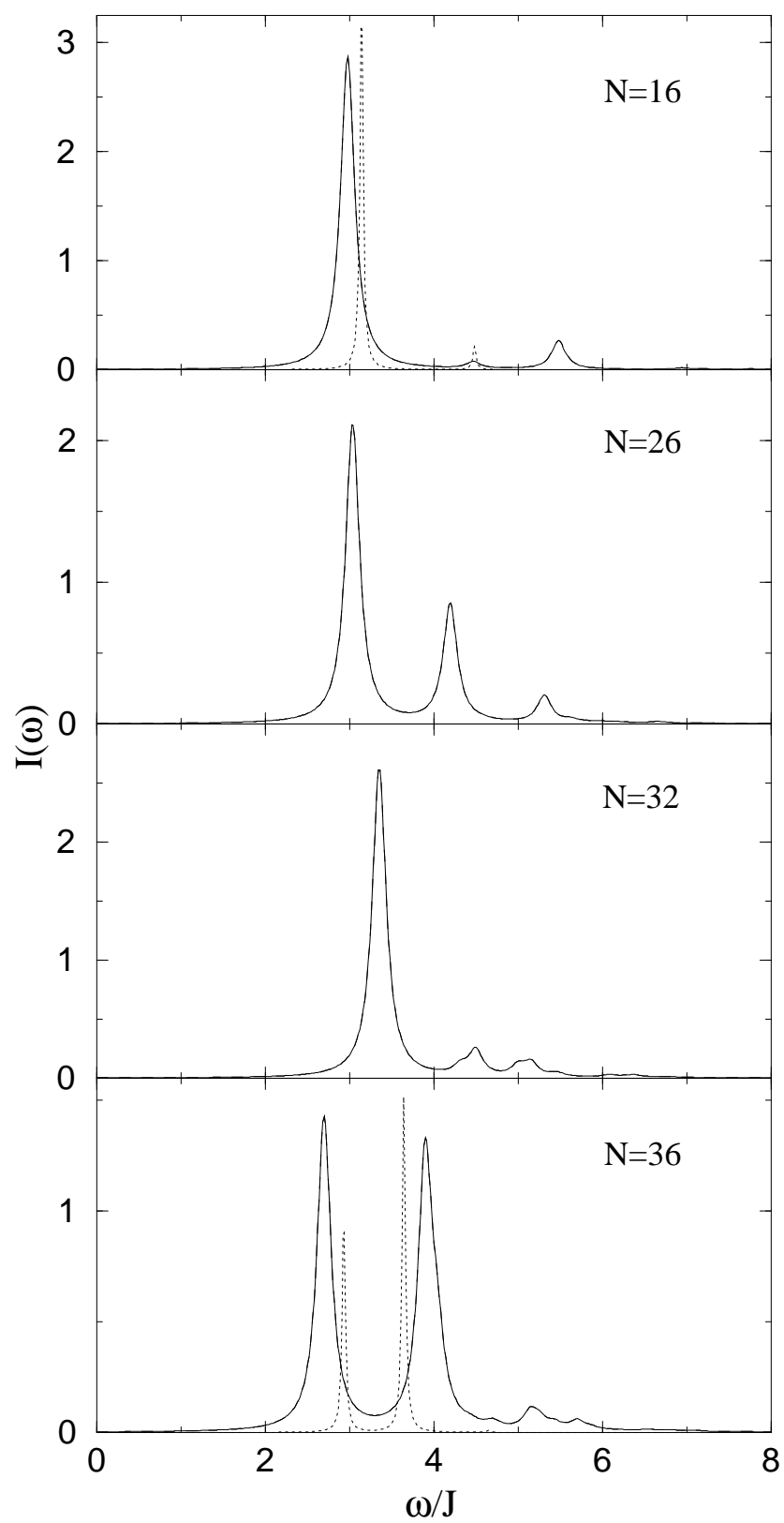


Fig. 3, A. W. Sandvik et al.

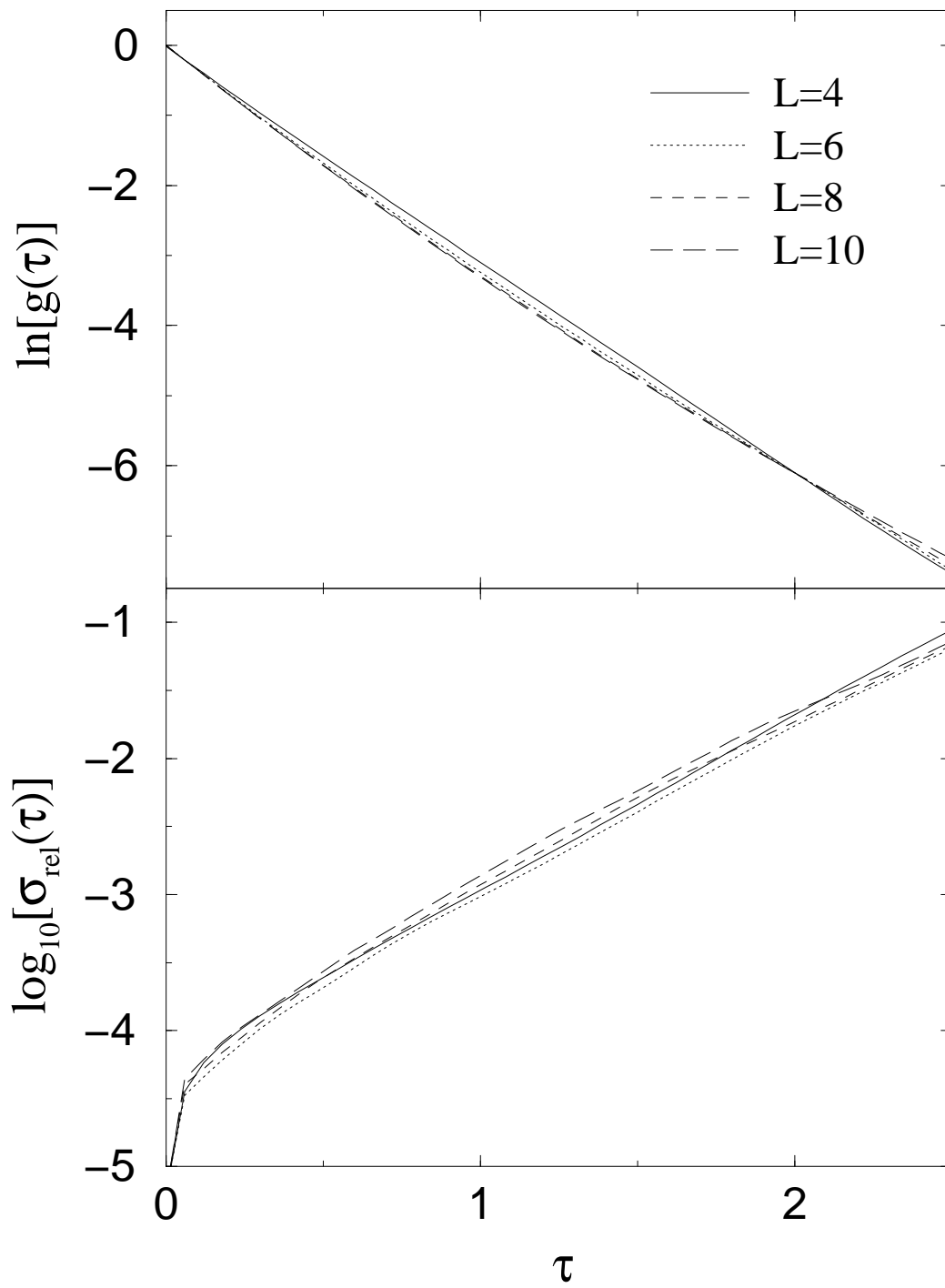


Fig. 4, A. W. Sandvik et al.

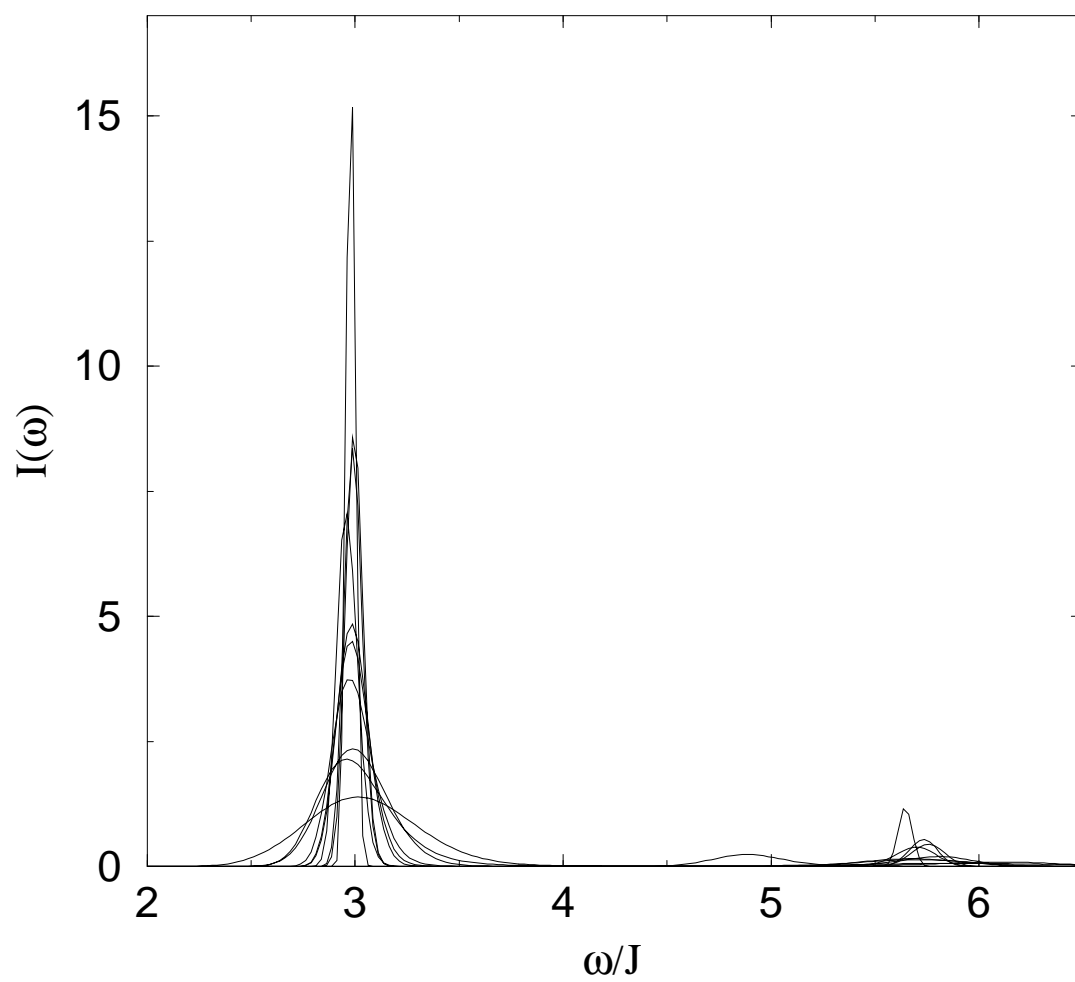


Fig. 5, A. W. Sandvik et al.

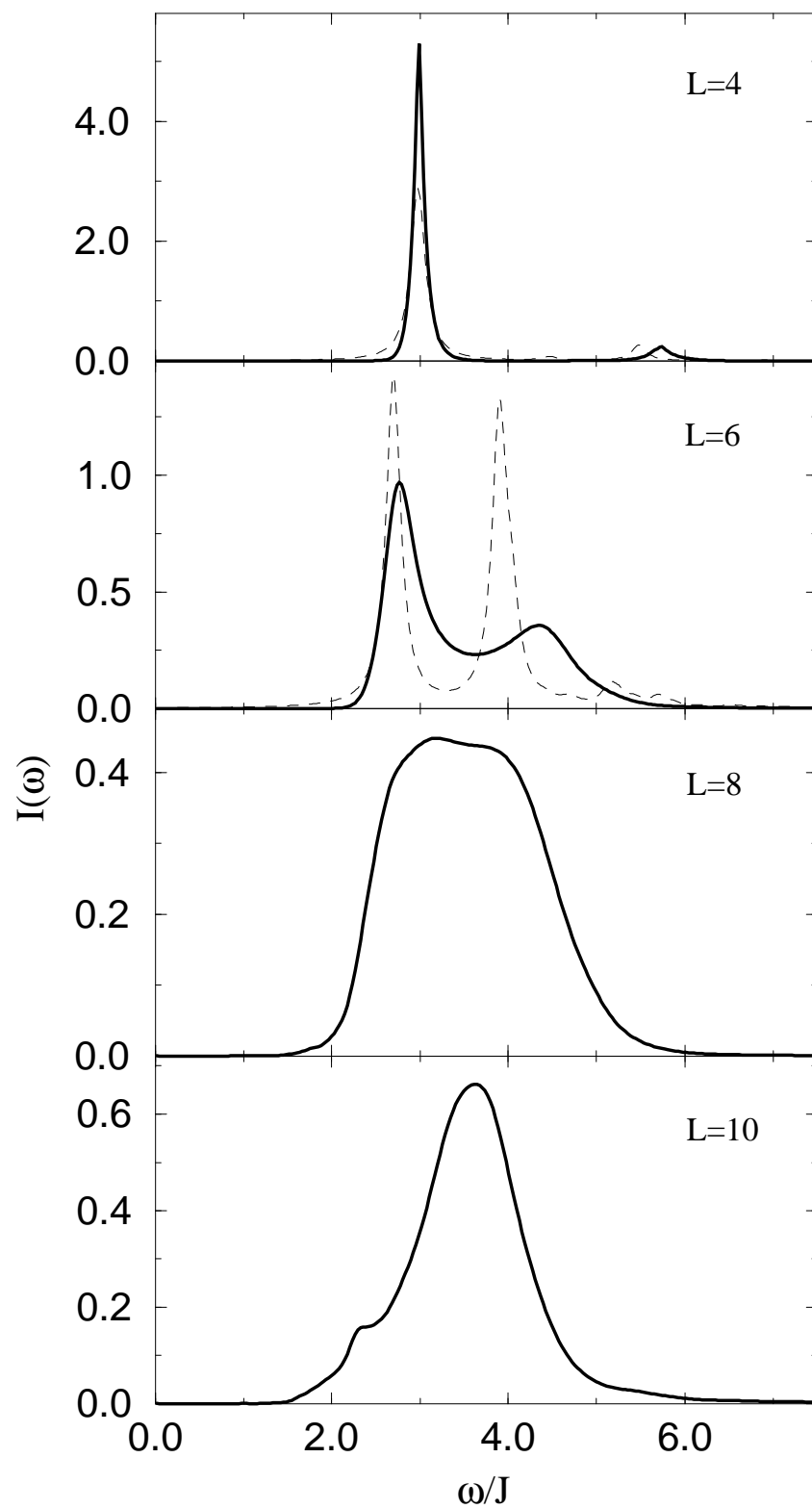


Fig. 6, A. W. Sandvik et al.

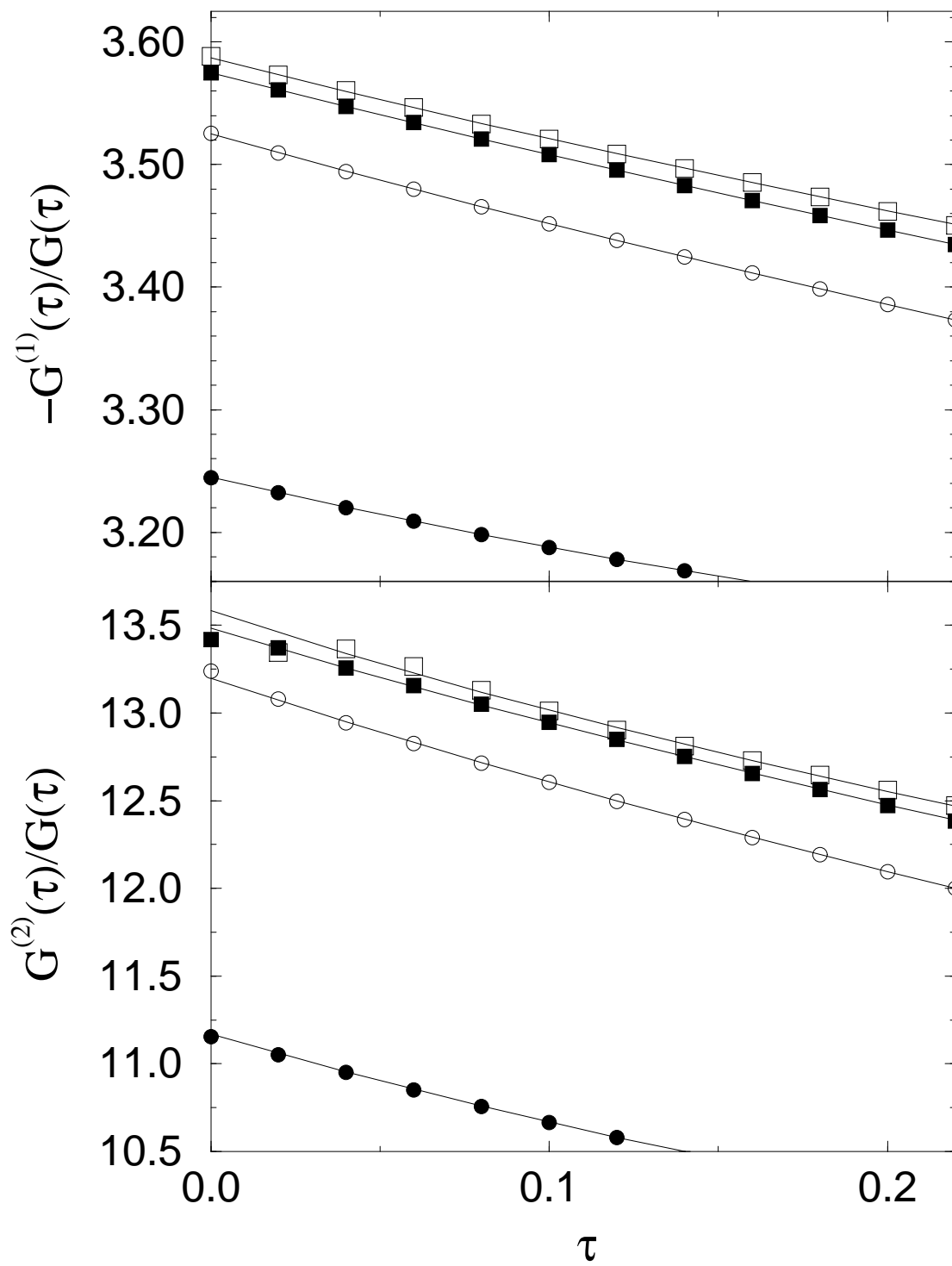


Fig. 7, A. W. Sandvik et al.

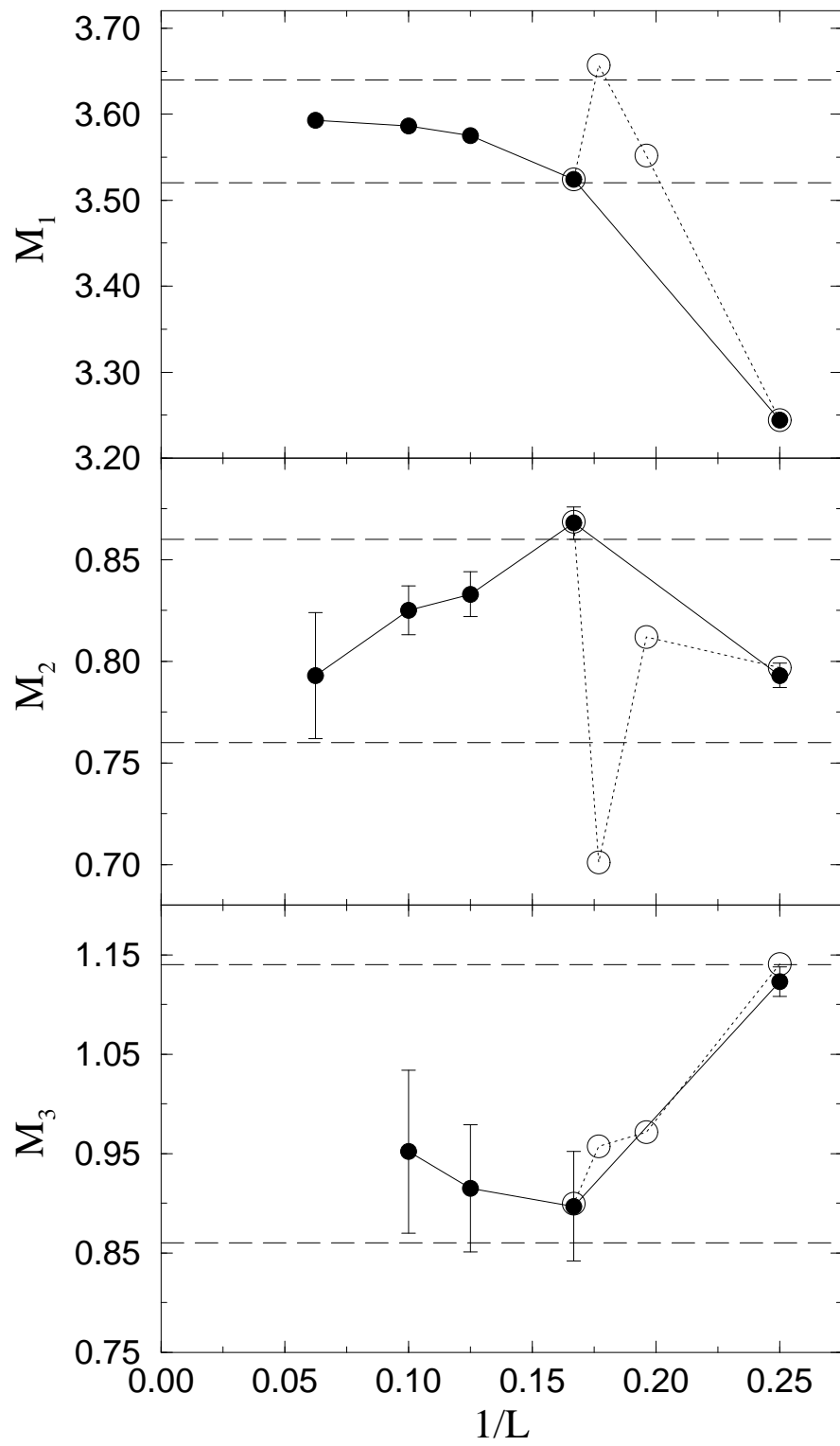


Fig. 8, A. W. Sandvik et al.

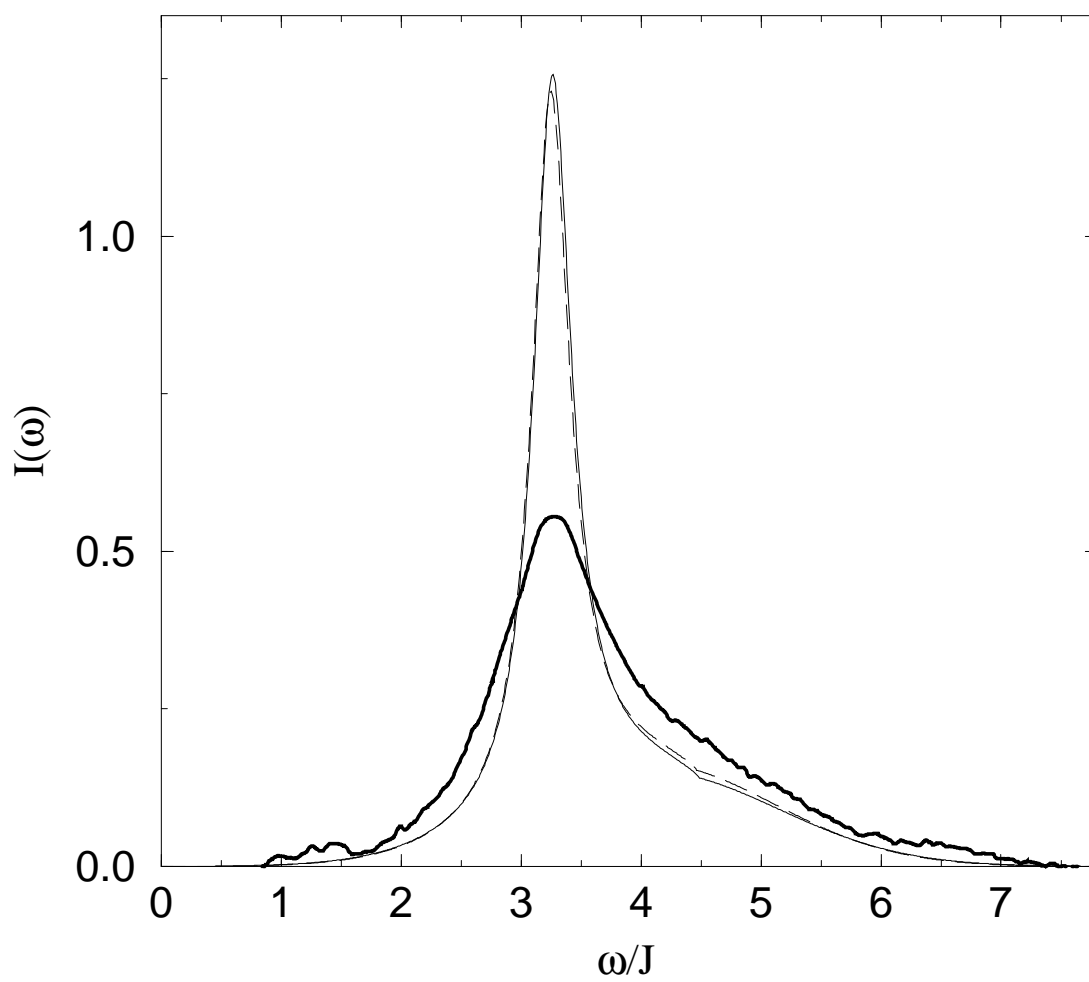


Fig. 9, A. W. Sandvik et al.

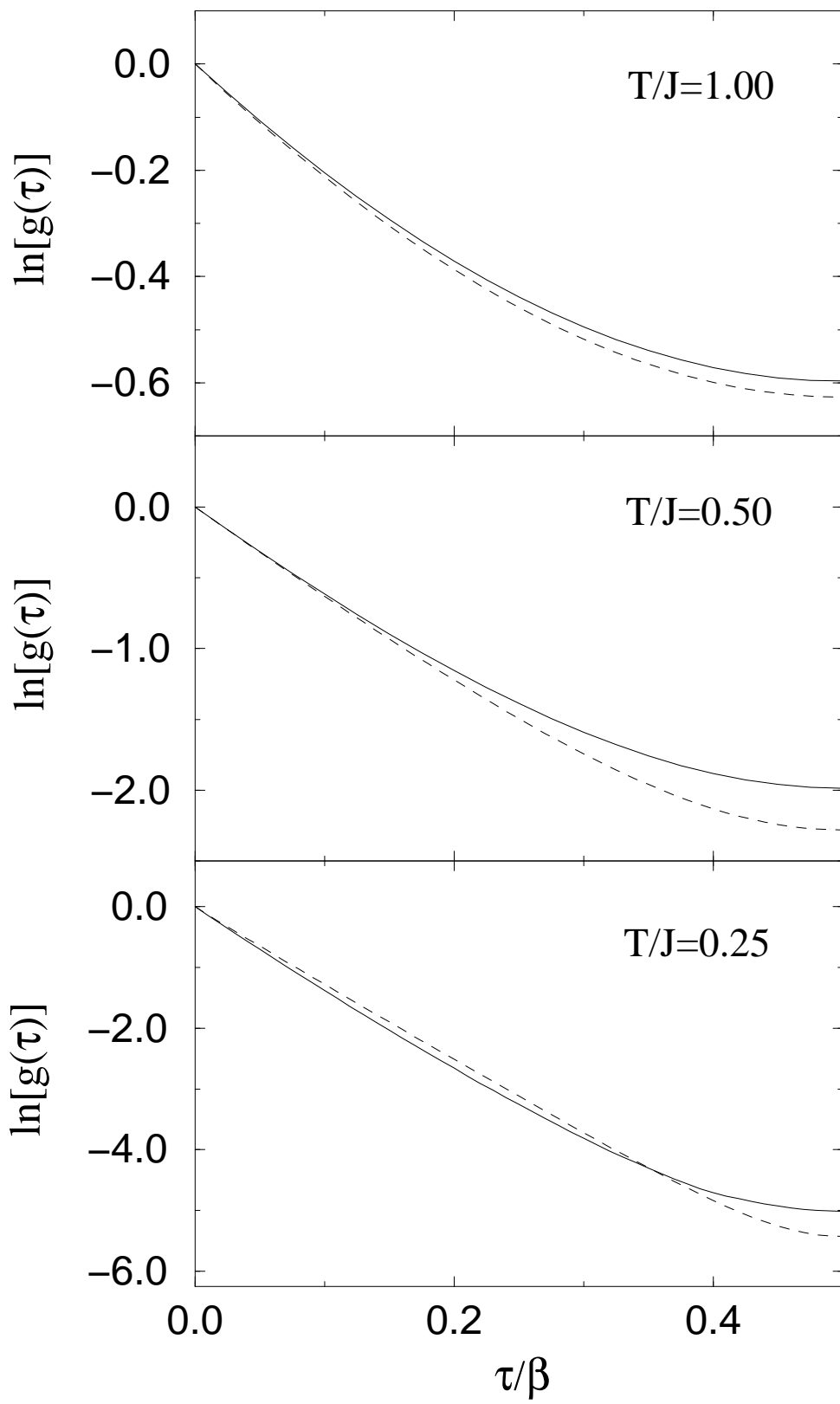


Fig. 10, A. W. Sandvik et al.

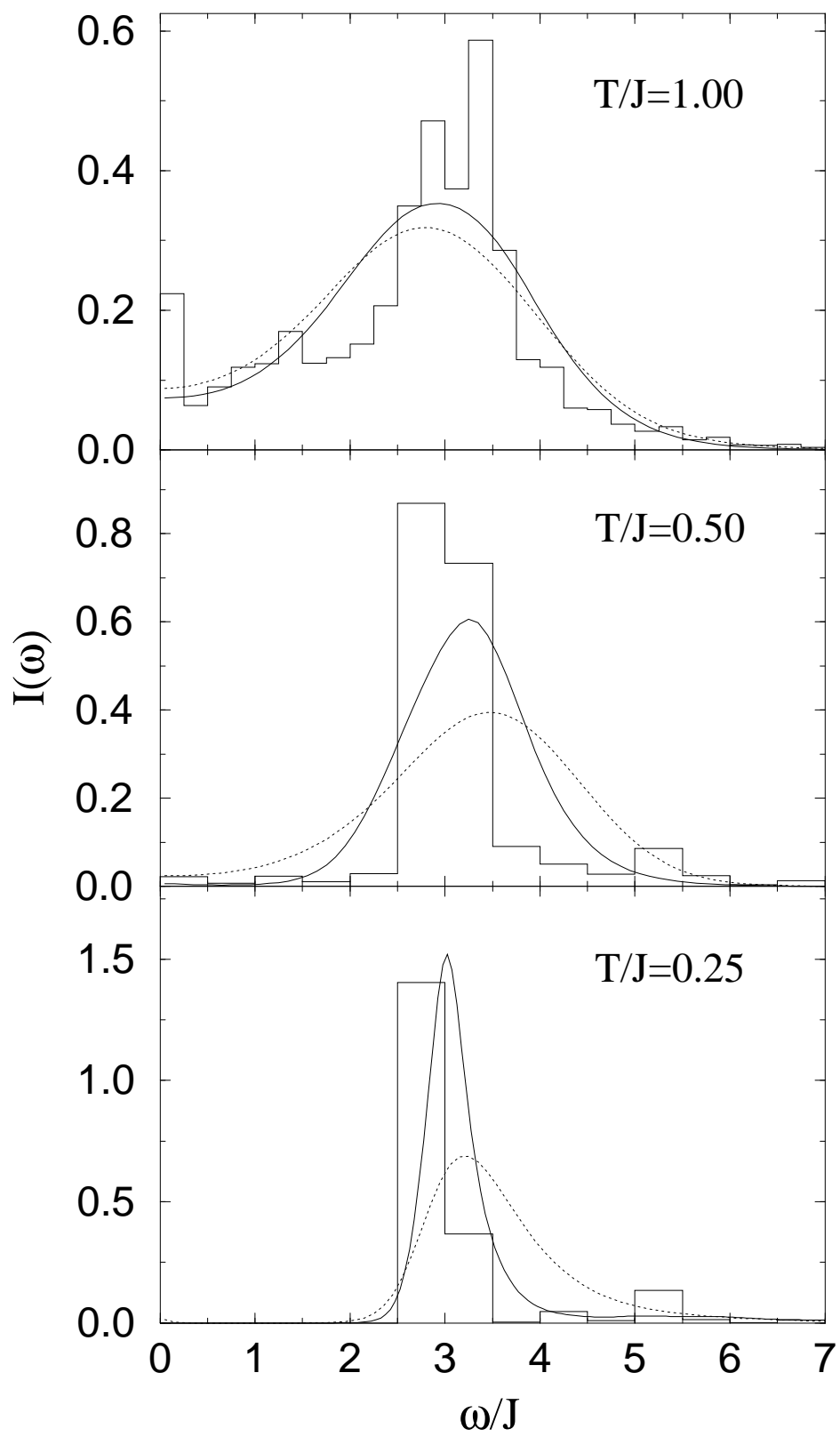


Fig. 11, A. W. Sandvik et al.

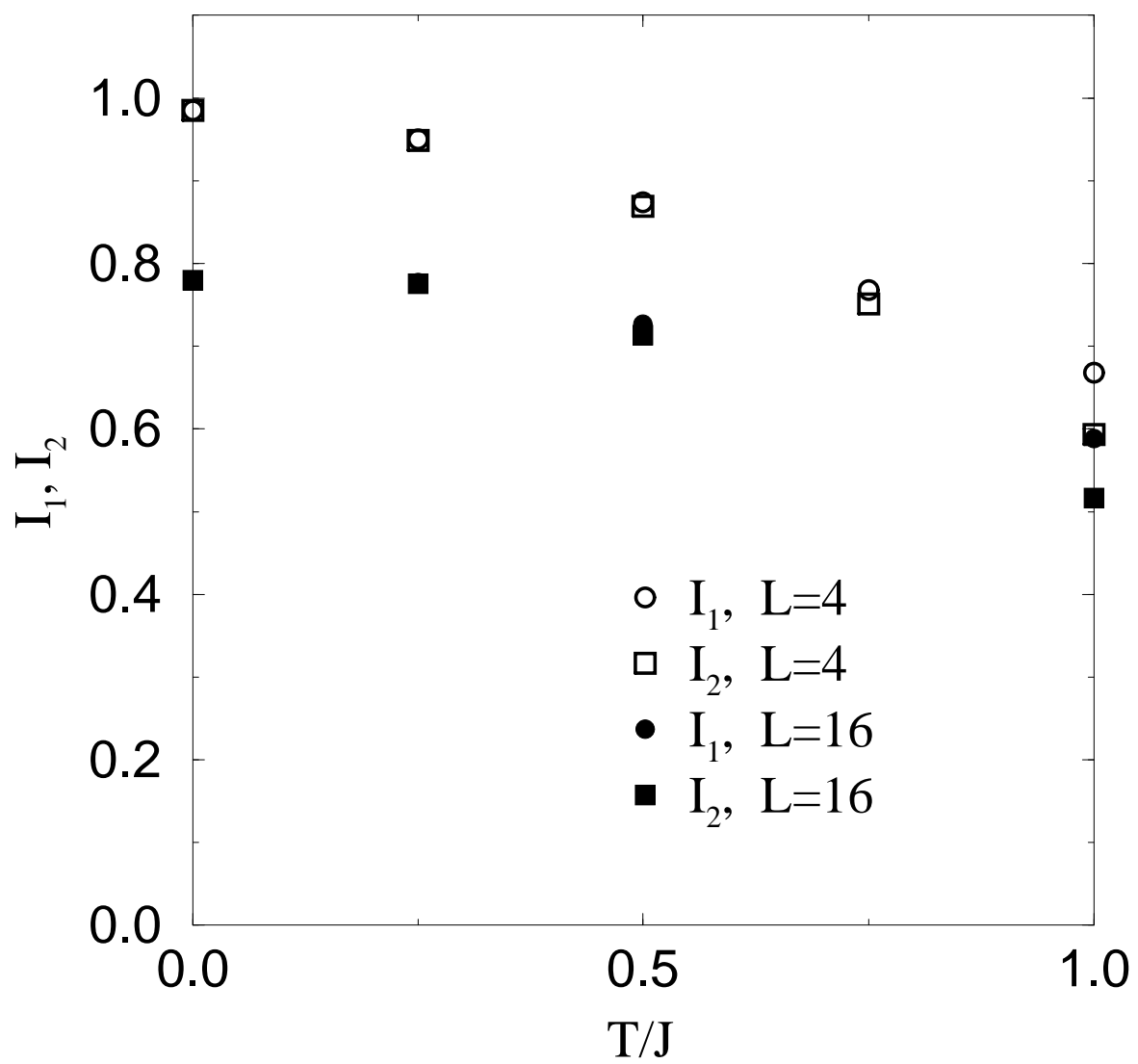


Fig. 12, A. W. Sandvik et al.

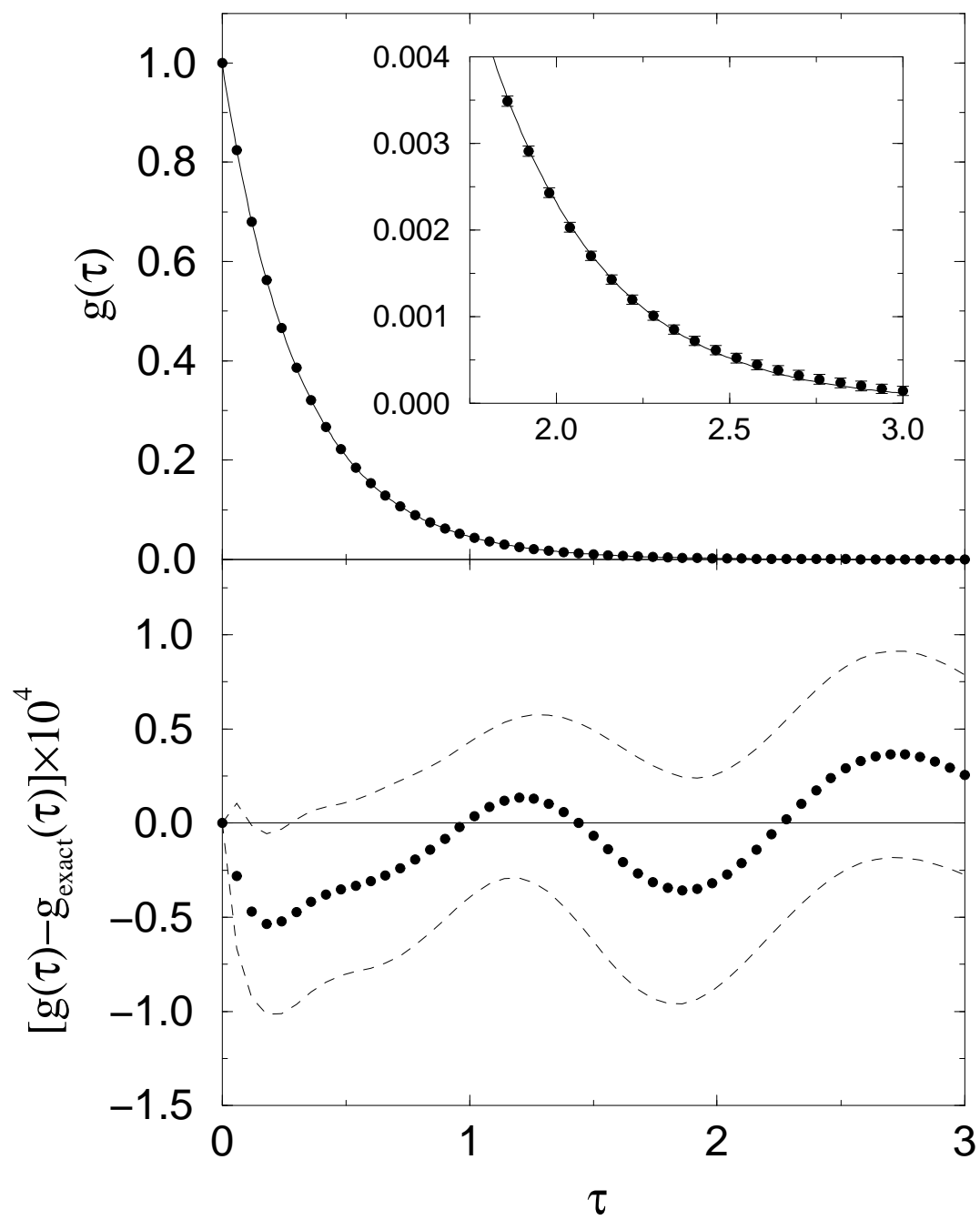


Fig. 13, A. W. Sandvik et al.